

AD-A244 049



①

AFIT/GAE/ENY/91D-25

DTIC  
ELECTE  
JAN 8 1992  
S D

THERMAL NONEQUILIBRIUM  
EFFECTS ON  
TURBINE CASCADE AERODYNAMICS

THESIS

Jill L. R. Shaw, Captain, USAF

AFIT/GAE/ENY/91D-25

92-00039



Approved for Public release; distribution unlimited

AFIT/GAE/ENY/91D-25

THERMAL NONEQUILIBRIUM EFFECTS ON  
TURBINE CASCADE AERODYNAMICS

THESIS

Presented to the Faculty of the School of Engineering  
of the Air Force Institute of Technology  
Air University  
In Partial Fulfillment of the  
Requirements for the Degree of  
Master of Science in Aeronautical Engineering

Jill L. R. Shaw, B.S.  
Captain, USAF

December 1991

Approved for public release; distribution unlimited



Table of Contents

	Page
Acknowledgements . . . . .	ii
List of Figures . . . . .	v
List of Tables . . . . .	vi
List of Symbols . . . . .	vii
Abstract . . . . .	x
I. Introduction . . . . .	1
I.1 Background . . . . .	1
I.2 Outline of Study . . . . .	2
I.3 Assumptions . . . . .	5
II. Theory and Analysis . . . . .	7
II.1 Governing Equations . . . . .	7
II.2 Finite-Difference Scheme . . . . .	12
II.3 Grid . . . . .	19
II.4 Boundary Conditions . . . . .	20
II.5 Initial Conditions . . . . .	22
III. Results . . . . .	26
III.1 Case Summary . . . . .	26
III.2 CFL Criteria and Norm Histories . . . . .	28
III.3 Blade Temperature Profiles . . . . .	34
III.4 Trailing Edge Temperatures . . . . .	38
III.5 Gamma Comparisons . . . . .	40
III.6 Computational Time Comparisons . . . . .	43
IV. Conclusions and Recommendations . . . . .	45
IV.1 Conclusions . . . . .	45
IV.2 Recommendations for Further Study . . . . .	46
Appendix A: Shock Tube Analysis . . . . .	47

Appendix B: Code Modification . . . . .	52
Appendix C: Code Input . . . . .	55
Bibliography . . . . .	57
Vita . . . . .	59

List of Figures

Figure	Page
1. Cell Interfaces and Cell Centers . . . . .	16
2. Grid for Rounded Trailing Edge Blade . . . . .	20
3. Region of Undefined Solution . . . . .	29
4. Convergence History for ATEC Case 1. . . . .	31
5. Convergence History for ANTEC Case 1. . . . .	31
6. Convergence History for ATEC Case 2 . . . . .	32
7. Convergence History for ANTEC Case 2 . . . . .	32
8. Convergence History for ATEC Case 3 . . . . .	33
9. Convergence History for ANTEC Case 3 . . . . .	33
10. Blade Temperature Profile Case 1 . . . . .	36
11. Blade Temperature Profile Case 2 . . . . .	36
12. Blade Temperature Profile Case 3 . . . . .	37
13. Expanded View Case 3 Temperature Difference at the Trailing Edge . . . . .	39
14. Expanded View Case 3 Temperature Difference Showing Shock Impact on Suction Surface . . . . .	39
15. Gamma Comparison for Case 1 . . . . .	41
16. Gamma Comparison for Case 2 . . . . .	41
17. Gamma Comparison for Case 3 . . . . .	42
18. Vibrational Temperature for Case 3 . . . . .	42
19. Shock Tube Results . . . . .	48
20. Conservation of Vibrational Energy . . . . .	54

List of Tables

Table	Page
1. Case Summary for Desired Inlet Conditions. . . . .	23
2. Case Summary for Inlet Mach and $\gamma$ . . . . .	24
3. Case Summary for Conditions Far Upstream . . . . .	25
4. Comparisions to Desired Inlet Conditions . . . . .	27
5. CFL Changes . . . . .	30
6. Computer Time Comparisons . . . . .	43

### List of Symbols

Symbol	Definition
$a$	eigenvalues of the Jacobian matrix
$A$	empirical constant for relaxation time
$A$	Jacobian Matrix
$B$	Jacobian Matrix
$c$	speed of sound
$D$	Roe averaging factor
$E$	energy per unit volume (will be subscripted)
$e$	energy (will be subscripted)
$E$	flux vector in the x-direction
$F$	flux vector in the y-direction
$f$	Numerical flux
$\tilde{g}$	the limiter
$H$	Enthalpy
$K$	constant based on metrics
$\mathcal{L}$	operator for Strang-type fractional step method
$M$	Mach number
$N$	norm
$P$	pressure
$Q_{\text{vib}}$	partition function of molecular vibration
$Q$	entropy correction factor
$R$	Eigenvector matrix
$R^{-1}$	inverse of the eigen value matrix
$\mathcal{R}$	Universal gas constant
$R$	gas constant

S	source vector
T	temperature
U	velocity
U	vector of dependent variables
u	velocity in the x-direction
$u_c$	contravariant velocity
v	velocity in the y-direction
$v_c$	contravariant velocity
W	relative gas velocity
$W_{vib}$	vibrational source term
$C_p$	specific heat at a constant pressure
$C_v$	specific heat at a constant volume
$\gamma$	ratio of specific heats
$\Delta_t$	time step
$\lambda$	$\Delta$ time/ $\Delta$ space
$\tau$	vibrational relaxation time
$\xi$	transformed coordinate
$\eta$	transformed coordinate
$\theta_v$	characteristic vibrational temperature
$\rho$	density
$\beta$	effective numerical viscosity
v	Courant number (without super- or subscripts)
$\mu$	reduces mass
$\kappa$	pressure derivative

### Subscript Definitions

2	inlet condition
3	exit condition
a	denotes original version of ATEC value
cr	condition at Mach number of unity
eff	effective value calculated from nonequilibrium flow
int	internal
ne	denotes ANTEC value
t	total
vib	dealing with the vibrational mode
x	differentiate with respect to x
y	differentiate with respect to y
$\xi$	differentiate with respect to $\xi$
$\eta$	differentiate with respect to $\eta$
$\infty$	far upstream

### Superscript Definitions

h	$\Delta_t$
n	time level

### Abstract

The AFIT Total Variation Diminishing Euler Code (ATEC) was modified to include a thermal nonequilibrium model to investigate high-temperature effects associated with vibrational relaxation in a transonic turbine cascade. Incorporation of this model into ATEC and creating ANTEC (AFIT Nonequilibrium TVD Euler Code) was accomplished in three phases. Steady-state solutions obtained with ANTEC were compared with those obtained with ATEC for various inlet and exit conditions. The CFL criterion was held constant in ATEC; however, it required variation for ANTEC. Blade temperature profiles, temperature difference contours in the vicinity of the trailing edge and the value of  $\gamma$  along the blade were analyzed. Even when corrected for high temperatures, the assumptions of a calorically perfect gas and thus a constant value of  $\gamma$  are inaccurate due to the temperature dependent nature of  $C_p$  and  $C_v$ . Maximum temperature differences of  $-741^\circ\text{K}$  and  $539^\circ\text{K}$  were found near the trailing edge for the highest temperature case, with differences being most noticeable through the expansion at the trailing edge on the pressure surface and across the shocks from both surfaces. The vibrational relaxation model showed limitations at low temperatures.

THERMAL NONEQUILIBRIUM EFFECTS ON  
TURBINE CASCADE AERODYNAMICS

I. Introduction

I.1 Background

Current algorithms used to model flow through transonic turbine engine cascades, including ATEC (AFIT Total Variation Diminishing (TVD) Euler Code), assume a perfect gas and neglect high-temperature effects such as molecular vibration, dissociation, and ionization. Across a shock wave, kinetic energy is converted to thermal energy. At high temperatures this thermal energy can vibrationally excite the air molecules. Ignoring such real gas effects can lead to an extreme miscalculation of flow temperatures. For example, using perfect gas theory for a blunt-nose insulated vehicle at 60,000ft ( $T_{\infty} = 390^{\circ}\text{R}/472^{\circ}\text{K}$ ) with a Mach number of 14, a temperature of over  $10,000^{\circ}\text{K}$  is predicted behind the shock (the surface of the sun is  $6,000^{\circ}\text{K}$ ). The temperature will actually be  $4,900^{\circ}\text{K}$  because molecules absorb energy in a real gas.

(13:549) Although existing transonic turbine cascades do not run at similar flow conditions, flows do reach temperatures where oxygen begins to dissociate ( $2000\text{--}2500^{\circ}\text{K}$  at one atmosphere of pressure) (2:19,374); above  $500^{\circ}\text{K}$  the specific heat at constant pressure,  $c_p$ , can no longer be assumed constant for diatomic molecules such as  $\text{O}_2$  and  $\text{N}_2$ . (3:63) Assuming that turbine cascades of the future will be running at even

higher temperatures than present ones, incorporation of a thermal nonequilibrium gas model into ATEC is an important first step towards more accurate simulations of transonic turbine flow fields.

This effort is a merging of research and code development recently completed at AFIT. ATEC, developed by Capt Mark Driver, is "an explicit, time-accurate, two-dimensional, finite-volume, Euler solver ... with the capability of resolving the complex shock structure in a typical transonic rotor cascade." (7:1) The code uses the TVD scheme developed by Harten as modified by Yee. (7,25) ATEC has demonstrated improved resolution over other second-order shock capturing schemes such as Lax-Wendroff, and comparisons to available experimental and analytical solutions have been favorable. (7:2) The selected thermal nonequilibrium model is identical to that developed by Capt Ken Moran in his investigation of hypersonic flow about a simple axisymmetric blunt-body at moderate hypersonic speeds. This model was developed for possible use with multi-species gases. (16,17) The purpose of this study is to investigate the thermal nonequilibrium effects and compare results assuming a perfect gas for turbine cascades.

## 1.2 Outline of Study

As with any problem, breaking this research into smaller pieces facilitated progress and understanding. Phase One consisted of implementing a second-order TVD scheme for a shock tube problem. Harten's ULTIC algorithm (12) was used due to its capability to accurately capture the shock and the contact surface. Harten also presents shock tube data with which comparisons could be made.

Although there is a strong interaction between molecular energy modes (15:4), a simpler model was investigated first; therefore, only the vibrational relaxation model was incorporated into the shock tube problem for Phase Two. Moran investigated two vibrational relaxation models: the Milliken and White model and the Park model. (16:22-24) The Milliken and White model computes relaxation times based on an empirical formula (Equations 9 and 10). The Park model incorporates the collision time and was developed for suborbital hypersonic flight. (19:440) The applicability of the Park model at moderate to low Mach numbers is not known. Therefore, the Milliken and White model was chosen for this investigation.

The TVD scheme used for the first and second phases, ULT1C, is based on a second-order accurate, upwind-differencing scheme. The unique character of TVD schemes is the numerical dissipation in the flux term. According to Yee (25), TVD schemes were developed for homogeneous hyperbolic problems and a nonequilibrium source term may or may not preserve the original TVD properties. However, if each species of a gas is assumed to behave as a thermally perfect gas, the flux function will possess the homogeneous property. (25:117) It is this flux function that makes the scheme stable and robust near flow field discontinuities, resulting in good shock capturing capability. The dissipation is locally adjusted and applied differently to the linearly degenerate fields and the genuinely nonlinear ones. Linearly degenerate fields are those in which  $a^k R^k = 0$  and are exclusively contact discontinuities; where  $a^k$  represents an eigenvalue,  $R^k$  represents an eigenvector of the Jacobian matrix (explained in Section II.2), and  $k$  is valued from 1 to 5

in this study. In contrast, nonlinear fields ( $a^k R^k \neq 0$ ) are either shocks or rarefaction waves. (12:374) With this form of numerical dissipation, the smearing of the contact surface and leading and trailing edges of the expansion fan is not as pronounced as with a first-order Roe scheme or the other second-order TVD schemes discussed by Harten. (12:380-393) The linearly degenerate fields are modified to be slightly convergent, thus reducing smearing and loss of resolution in the contact discontinuity region. The characteristic fields corresponding to the eigenvalue  $U$  are linearly degenerate and the fields corresponding to  $U \pm C$  are genuinely nonlinear. (12:379)

Phase Three saw the merging of the relaxation model into ATEC, which uses Yee's modification to ULT1C due to the over diffusive nature of ULT1C in two dimensions. (8,25:25) This is also a shock capturing scheme that eliminates the need to know a priori the complex shock structure in a turbine cascade. In general, classical shock capturing schemes have resulted in non-physical oscillations near discontinuities. In contrast, these oscillations are not observed with TVD schemes. The modified version will be referred to as ANTEC (AFIT Nonequilibrium TVD Euler Code).

At this point, comparisons between ATEC and ANTEC were made at various flow conditions to determine any 'high-temperature' effects. First, a low-temperature, low-pressure case was used for debugging and verification of ANTEC. Even though the blade geometry was for a transonic rotor cascade designed by NASA and not that of a F100 turbine blade, the F100-PW turbine's inlet temperature, pressure, and stage pressure ratio were chosen for the next case as being representative of

turbine conditions. Actual numbers for turbines currently in design were not available due to their sensitive nature. This research was concerned with the concept of thermal nonequilibrium effects in the flow through a turbine cascade. The NASA blade geometry and the F100-PW turbine conditions simulate a hypothetical turbine for research purposes. Once the F100 inlet case was run, the inlet temperature was increased, holding the other factors constant to investigate any high-temperature effects; such as temperature differences between the two codes. These differences were seen to be greatest in the vicinity of the trailing edge.

### 1.3 Assumptions

Throughout this study certain assumptions were made to simplify the problem:

1. Air is a single "composite" species approximately consisting of 21% O<sub>2</sub> and 79% N<sub>2</sub> with a molecular weight of 28.9844 kg/kg-mole. (20:87)
2. The gas is thermally perfect.
3. The effects of molecular transport (viscosity, diffusion, thermal conductivity) are negligible. (22:178)
4. There are no dissociation, ionization or electronic effects.
5. All energy modes decouple.

For an analysis based on a multi-species gas, a continuity equation and vibrational energy equation are necessary for each species. (16,17) Therefore, the first assumption simplifies the structure of the governing equations. A thermally perfect gas has a constant value of R;

however, the specific heats,  $c_p$  and  $c_v$ , and their ratio,  $\gamma$ , are not necessarily constant. The assumption of a thermally perfect gas also allows retention of the desired TVD properties. (25:117) The remaining assumptions serve to more fully isolate nonequilibrium effects due to molecular vibration. The degree of dissociation of a gas will decrease as pressure increases, making the fourth assumption valid for a high-temperature, high-pressure turbine cascade (approximately 20 atmospheres at the inlet). (22:152-157)

Yee discusses second-order TVD applications for nonequilibrium flows (25:115-117) which were applied by Moran in his research of thermal and chemical nonequilibrium flows in a one-dimensional shock tube. (17) Unfortunately, no literature was found that dealt with nonequilibrium flow through a turbine cascade. Also limited experimental data for flow through a turbine cascade was found that could possibly be used for comparisons. (6,9) In the data that was found, there were significant radial pressure gradients across the duct. ATEC could be modified to account for variations at the inlet; however, it was felt that a more systematic comparison of ATEC and ANTEC could be obtained without changing the inflow conditions.

## II. Theory and Analysis

### II.1 Governing Equations

Since a weak solution is anticipated, the conservative or divergence form of the governing Euler equations is used. This choice also simplifies the derivation of a second-order explicit algorithm. (23:87) The governing equations in conservation form are

$$\frac{\partial U}{\partial t} + \frac{\partial E(U)}{\partial x} + \frac{\partial F(U)}{\partial y} = S \quad (1)$$

where

$$U = \begin{bmatrix} \rho \\ \rho u \\ \rho v \\ E_t \\ E_{vib} \end{bmatrix} \quad E = \begin{bmatrix} \rho u \\ \rho u^2 + P \\ \rho uv \\ (E_t + P)u \\ E_{vib}u \end{bmatrix} \quad F = \begin{bmatrix} \rho v \\ \rho uv \\ \rho v^2 + P \\ (E_t + P)v \\ E_{vib}v \end{bmatrix} \quad S = \begin{bmatrix} 0 \\ 0 \\ 0 \\ 0 \\ W_{vib} \end{bmatrix} \quad (2)$$

These are the Euler equations for conservation of mass, momentum and energy for an inviscid, non-conducting gas plus a fifth equation to account for the decoupled vibrational energy. The source term,  $W_{vib}$  (defined in Equation 8), is the Landau-Teller form describing the energy exchange between energy modes, which assumes that molecules are free to vibrate in any quantum level, but changes in energy only occur with

adjacent levels. (3:65,17:8)  $E_t$  is the total energy per unit volume as defined by

$$E_t = \frac{P}{(\gamma-1)} + \frac{\rho}{2} (u^2+v^2) + E_{vib} \quad (3)$$

$E_{vib}$  is the vibrational energy per unit volume ( $E_{vib} = e_{vib}\rho$ ). The equilibrium model characterizing vibrational energy,  $e_{vib}$ , is based on statistical and quantum mechanics. (22:86-139) This model states that all internal energy is partitioned into translational, rotational, vibrational and electronic modes. The equilibrium vibrational energy is given by the equation

$$e_{vib} = RT^2 \frac{\partial (\ln Q_{vib})}{\partial T} \quad (4)$$

with  $Q_{vib}$  being the partition function

$$Q_{vib} = \frac{1}{1 - \exp \frac{-\theta_v}{T}} \quad (5)$$

After substitution of Equation 5 into the equilibrium equation for vibrational energy, Equation 4 becomes

$$e_{vib} = \frac{R \theta_v}{\exp \frac{\theta_v}{T} - 1} \quad (6)$$

The characteristic vibrational temperature,  $\theta_v$ , is a constant obtained from spectroscopic data. The value used in this study ( $\theta_v = 3154.8^\circ\text{K}$ ) is a mole weighted value from the assumption made in Section I.3 that air is made up of  $\text{O}_2$  ( $\theta_v = 2270^\circ\text{K}$ ) and  $\text{N}_2$  ( $\theta_v = 3390^\circ\text{K}$ ). (22:135)

$W_{\text{vib}}$  is a function of the relaxation time,  $\tau$ . Relaxation time can be considered the time necessary for molecules in nonequilibrium (for example, air through a shock) to absorb energy and reach an equilibrium state. The rate at which the gas will approach equilibrium is directly proportional to its departure from equilibrium. (11:196)

As with Moran's previous nonequilibrium analyses (16,17), this study will use a two-temperature model. The first temperature,  $T$ , identifies the translational/rotational energy in equilibrium and the second temperature,  $T_{\text{vib}}$ , identifies the nonequilibrated vibrational energy. Equilibrium exists when  $T$  and  $T_{\text{vib}}$  are equal, in which case the source term,  $W_{\text{vib}}$ , will be zero.

$$T_{\text{vib}} = \frac{\theta_v}{R \frac{\theta_v}{e_{\text{vib}}} + 1} \quad (7)$$

$W_{\text{vib}}$  is defined as (17:8)

$$W_{\text{vib}} = \rho \frac{e_{\text{vib}T} - e_{\text{vib}T_{\text{vib}}}}{\tau} \quad (8)$$

with  $e_{\text{vib}T}$  being the vibrational energy defined by Equation 6 and  $e_{\text{vib}T_{\text{vib}}}$  is extracted from the solution of  $E_{\text{vib}}$ . Vibrational relaxation times have

been determined experimentally; and below 5000°K, it has been shown that for the most common species in air,  $\tau$  can be determined by (18:58)

$$\tau = \frac{\exp(A (T^{-1/3} - .015\mu^{1/4}) - 18.42)}{P} \quad (9)$$

$$A \equiv 1.16 \times 10^{-3} \mu^{-1/2} \theta_v^{4.3} \quad (10)$$

$\mu$  is called the reduced mass of the air. For the single species case, it becomes one-half of the molecular weight.  $T$  defines the translational/rotational energy and is given by

$$T = \frac{P}{\rho R} \quad (11)$$

$$P = (\gamma - 1) [E_t - E_{vib} - \frac{\rho}{2} (u^2 + v^2)] \quad (12)$$

In determining  $\tau$ ,  $P$  is pressure in atmospheres. Pressures in the codes were in  $N/m^2$ , so that a conversion factor of 101,325  $N/m^2/atm$  was implemented to incorporate Equation 9 into ANTEC. Clearly, as  $P$  increases the relaxation time will decrease.

$R$  is the gas constant defined by

$$R = \frac{\mathcal{R}}{\text{molecular weight}} \quad (13)$$

$\mathcal{R}$  being the Universal Gas Constant equal to 8134  $J/^\circ K \text{ mole}$ .

Remembering that the value of  $c_p$  is temperature dependant and with the assumption of a thermally perfect gas, an equilibrium or effective value of  $\gamma$  can be calculated using the following relationships

$$\gamma = \frac{c_p}{c_v} \quad (14)$$

and

$$c_p = c_v + R \quad (15)$$

where

$$c_v = c_{v_{\text{Trans/Rot}}} + c_{v_{\text{Vib}}} \quad (16)$$

$\gamma$  can be solved for using

$$c_{v_{\text{Trans/Rot}}} = \frac{5}{2} R \quad (17a)$$

(22:124,133) and

$$c_{v_{\text{Vib}}} = R \left( \frac{\theta_v}{T} \right)^2 \frac{\exp(\theta_v/T)}{(\exp(\theta_v/T) - 1)^2} \quad (17b)$$

(22:135) In the limit as  $T$  approaches zero,  $c_{v_{\text{Vib}}}$  also goes to zero resulting in  $\gamma$  approaching 1.4. As  $T$  increases, the value of  $\gamma$  decreases; and as  $T$  becomes larger than  $T_{\text{vib}}$ ,  $c_{v_{\text{Vib}}}$  approaches  $R$ , indicating a fully excited state. If the temperature were to continue to increase, the energy would have to go into alternate modes such as electronic or dissociation. In equilibrium,  $c_v$  is dependant upon only one temperature,  $T$ . However, for this research, a generalization for application to nonequilibrium flow is necessary for comparison and  $c_{v_{\text{Vib}}}$

(Equation 17) will be defined using  $T_{vb}$  (Equation 7). With these, a value of  $\gamma$  can be constructed for a nonequilibrium flow. This will be referred to as  $\gamma_{eff}$ . The values of  $\gamma$  actually used in the codes will be referred to as  $\gamma_a$  for ATEC and  $\gamma_{ne}$  for ANTEC. For equations that are applicable to both codes,  $\gamma$  will be unsubscripted. When the equation is applied for ATEC,  $\gamma_a$  will be used; and conversely, when applied to ANTEC,  $\gamma_{ne}$  will be used.

Again, this research is only concerned with vibrational energy and relaxation. However, it should be noted, as a point of reference, that translational equilibrium is reached within a few collisions and rotational equilibrium is attained in less than ten collisions for most polyatomic gases; but vibrational equilibrium may require thousands of collisions. (14:25,3:62) So, for practical purposes, translational and rotational states can be considered to be in equilibrium instantaneously, whereas, vibrational relaxation requires a finite amount of time, which is approximated by  $\tau$ .

Appendix B briefly summarizes the modifications made to ATEC to create ANTEC.

## II.2 Finite-Difference Scheme

TVD is a class of modern higher-order shock capturing algorithms which uses nonlinear numerical dissipation to yield a stable, nonoscillatory solution. (25) Yee emphatically points out that the TVD property is only valid for homogeneous scalar hyperbolic problems. However, the TVD method has been successfully extended to the treatment of nonlinear systems of hyperbolic conservation laws. (25,7,17)

In the formulation of a TVD scheme, it is necessary to locally obtain the set of eigenvalues,  $\mathbf{a}$ , the eigenvector matrix,  $\mathbf{R}$ , and its inverse,  $\mathbf{R}^{-1}$ , for the two Jacobian matrices:

$$\mathbf{A} \equiv \frac{\partial E(\mathbf{U})}{\partial \mathbf{U}} \quad \mathbf{B} \equiv \frac{\partial F(\mathbf{U})}{\partial \mathbf{U}} \quad (18a,b)$$

Fortunately, these quantities are available in the literature. (7,16,25,12,15) However, it is also possible to solve for  $\mathbf{a}$ ,  $\mathbf{R}$ , and  $\mathbf{R}^{-1}$  using Mathematica if necessary. The eigenstructure of the original version of ATEC was extracted from Yee. (25,7,8) The nonequilibrium version incorporated the eigenstructure presented by Moran. (16:79-80) The eigenvalues for  $\mathbf{A}$ , following a general coordinate transformation, are

$$\mathbf{a} = \begin{bmatrix} u_c \\ u_c \\ u_c \\ u_c - K_\xi c \\ u_c + K_\xi c \end{bmatrix} \quad (19)$$

The eigenvector matrix of  $\mathbf{A}$  is

$$\mathbf{R} = \begin{bmatrix} 0 & 0 & 1 & 1 & 1 \\ -k_2 & 0 & u_c & u_c - k_1 c & u_c + k_1 c \\ k_1 & 0 & v_c & v_c - k_2 c & v_c + k_2 c \\ (k_1 v_c - k_2 u_c) & 1 & u_c^2 + v_c^2 & H - k_1 u_c c - k_2 v_c c & H + k_1 u_c c + k_2 v_c c \\ 0 & 1 & 0 & e_{vib} & e_{vib} \end{bmatrix} \quad (20)$$

and its inverse

$$R^{-1} = \begin{bmatrix} k_2 u + k_1 v & -k_2 & k_1 & 0 & 0 \\ -e_{\text{vib}} b_1 & u(e_{\text{vib}} b_2) & v(e_{\text{vib}} b_3) & -e_{\text{vib}} b_3 & 1 + e_{\text{vib}} b_3 \\ 1 - b_1 & u b_3 & v b_3 & -b_3 & b_3 \\ \left( \frac{b_1 + \frac{k_1 u + k_2 v}{c}}{2} \right) & \left( \frac{-b_3 u - \frac{k_1}{c}}{2} \right) & \left( \frac{-b_3 v - \frac{k_2}{c}}{2} \right) & \frac{b_3}{2} & \frac{-b_3}{2} \\ \left( \frac{b_1 - \frac{k_1 u + k_2 v}{c}}{2} \right) & \left( \frac{-b_3 + \frac{k_1}{c}}{2} \right) & \left( \frac{-b_3 + \frac{k_2}{c}}{2} \right) & \frac{b_3}{2} & \frac{-b_3}{2} \end{bmatrix} \quad (21)$$

where

$$b_3 = \frac{(\gamma - 1)}{c^2} \quad b_1 = b_3 \left( \frac{u^2 + v^2}{2} \right) \quad (22, 23)$$

$$k_1 = \frac{\xi_x}{(\xi_x^2 + \xi_y^2)^{\frac{1}{2}}} \quad k_2 = \frac{\xi_y}{(\xi_x^2 + \xi_y^2)^{\frac{1}{2}}} \quad (24, 25)$$

The contravariant velocity in the  $\xi$ -coordinate direction,  $u_c$ , is determined by

$$u_c = \xi_x u + \xi_y v \quad (26)$$

$$K_\xi = (\xi_x^2 + \xi_y^2)^{\frac{1}{2}} \quad (27)$$

where the speed of sound is  $c$ , defined by

$$c^2 = (\gamma - 1) \left( H - \frac{1}{2}(u^2 + v^2) - e_{vib} \right) \quad (28)$$

Enthalpy, H, is given by

$$H = \frac{(E_t + P)}{\rho} \quad (29)$$

In the  $\eta$ -coordinate direction,  $v_c$  is used in place of  $u_c$ , and  $\eta$  replaces  $\xi$  in all derivatives (Equations 19 and 24-27). The eigenvector matrix of  $B$  and its inverse have the same form as Equations 20 and 21, again using  $\eta$ -coordinate derivatives in Equations 24 and 25.

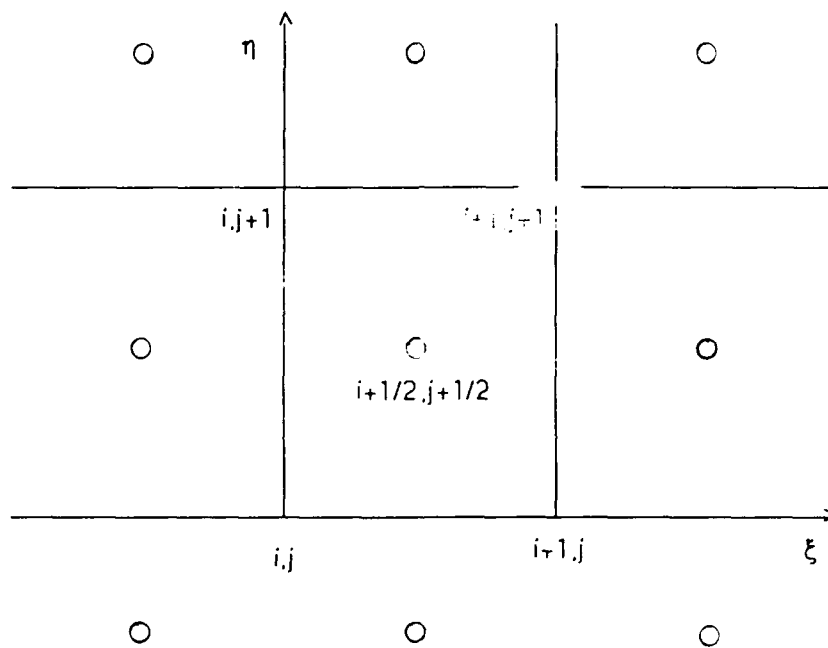
With the solution being generated at cell centers, Roe averaging was applied throughout the analysis since the eigenvalues and eigenvectors require some form of averaging at cell interfaces. This is the most common form of averaging due to its simplicity and its ability to resolve discontinuities. (25:59,6:5) Figure 1 depicts the cell interfaces  $(i,j)$ , cell centers  $(i+1/2,j+1/2)$ , and the cell centers outside of the boundaries known as ghost points. Roe averaging in one dimension is implemented by

$$x_{j+1/2} = \frac{D x_{j+1} + x_j}{D + 1} \quad (30)$$

where  $x$  is  $u$ ,  $v$ ,  $H$  or  $e_{vib}$ , and  $D$  is defined as follows

$$D \equiv \left( \frac{\rho_{j+1}}{\rho_i} \right)^{\frac{1}{2}} \quad (31)$$

Although the form of  $D$  chosen was for a perfect gas in equilibrium, it can still be used in this application due to the assumption of a thermally perfect gas. (25:59) This method of averaging was also discussed for nonequilibrium flows by Liu and Vinokur. (15:17)



Cell Centers Outside of Boundary (Ghost Points)

Figure 1: Cell Interfaces and Cell Centers

For simplification, the finite-difference scheme will only be developed in one dimension.

$$U_j^{n+1} = U_j^n - \lambda (\bar{f}_{j+1/2}^n - \bar{f}_{j-1/2}^n) + \Delta_t S \quad (32)$$

with  $\lambda$  defined as  $\Delta_t/\Delta\eta$  and  $\Delta_t S$  is the treatment of the source term. The  $n$  superscript is now dropped for simplicity. The numerical flux,  $\bar{f}_{j+1/2}$ , is evaluated at cell interfaces and is expressed as

$$\bar{f}_{j+1/2} = \frac{1}{2} \left[ F(U_j) + F(U_{j+1}) + \frac{1}{\lambda} \sum_{k=1}^m R_{j+1/2}^k \beta_{j+1/2} \right] \quad (33)$$

For this research  $m$  was 5.  $R_{j+1/2}^k$  are the eigenvectors; and the effective numerical viscosity,  $\beta_{j+1/2}$ , is defined as

$$\beta_{j+1/2} = \sigma(v_1^k)_{j+1/2} (\bar{g}_j + \bar{g}_{j+1}) - Q(v_2^k) \alpha_{j+1/2}^k \quad (34)$$

with

$$v_2^k = \lambda a_{j+1/2}^k + \gamma_{j+1/2}^k \quad (35)$$

$$v_1^k = \lambda a_{j+1/2}^k \quad (36)$$

and

$$\alpha_{j+1/2}^k = \left( R_{j+1/2}^k \right)^{-1} \Delta_{j+1/2} U \quad (37)$$

$$\Delta_{j+1/2} U = U_{j+1} - U_j \quad (38)$$

$Q$ , the entropy correction factor or also known as the coefficient of numerical viscosity (12:363), and  $\sigma$  are functions expressed as

$$\sigma_{j+1/2}^k(z) = \frac{1}{2} (Q(z) - z^2) \quad (39)$$

$$Q(z) = \frac{z^2}{4\epsilon} + \epsilon \quad \text{for } |z| < 2\epsilon \quad (40)$$

$$Q(z) = |z| \quad \text{for } |z| \geq 2\epsilon$$

$\epsilon$  is a variable parameter in the code that can be selected by the user. Values between 0 and 1/2 are allowed; with 0 yielding the least dissipative results. (12:375,25:16)

For the linearly degenerate fields  $\tilde{g}_j^k$ , the limiter, is determined from

$$\tilde{g}_j^k = S_{j+1/2}^k \max[0, \min\{\omega_{j+1/2}^k |\alpha_{j+1/2}^k|, S_{j+1/2}^k \alpha_{j-1/2}^k, \min(|\alpha_{j+1/2}^k|, S_{j+1/2}^k \omega_{j+1/2}^k \alpha_{j-1/2}^k)\}] \quad (41)$$

with

$$S_{j+1/2}^k = \text{sign}(1, \alpha_{j+1/2}^k) \quad (42)$$

The 'sign' function assigns the sign (+ or -) of the second term in the parentheses to the value of 1.

$\omega$  is also an input parameter. Input into the codes is explained in Appendix C.

For the nonlinear fields

$$\tilde{g}_j^k = \frac{\alpha_{j+1/2}^k \alpha_{j-1/2}^k + |\alpha_{j+1/2}^k \alpha_{j-1/2}^k|}{\alpha_{j+1/2}^k + \alpha_{j-1/2}^k} \quad (43)$$

With Equations 37, 39, and 43,  $\gamma_{j+1/2}^k$  is obtained from

$$\gamma_{j+1/2}^k = \sigma(v_{j+1/2}^k) \frac{(\tilde{g}_{j+1}^k - \tilde{g}_j^k)}{\alpha_{j+1/2}^k} \quad \text{for } \alpha_{j+1/2}^k \neq 0 \quad (44a)$$

$$\gamma_{j+1/2}^k = 0 \quad \text{for } \alpha_{j+1/2}^k = 0 \quad (44b)$$

Here,  $\gamma$  is not related to the ratio of specific heats; use of this symbology is made to remain consistent with the literature. (25,12,7)

The Strang-type, fractional step method is incorporated to advance the solution in time (7:5)

$$U_{(i,j)}^{n+2} = \mathcal{L}_{\xi}^{h/2} \mathcal{L}_{\eta}^h \mathcal{L}_{\xi}^h \mathcal{L}_{\eta}^h \mathcal{L}_{\xi}^{h/2} U_{(i,j)}^n \quad (45)$$

where  $\mathcal{L}$  is an operator representing Equation 32,  $h = \Delta t$  and  $\xi$  and  $\eta$  correspond to the direction of the computational sweep. With this method, each iteration encompasses two time steps.

### II.3 Grid

The computational grid for this study was a C-type with 170x20 points. Since averaging at cell centers was required, a grid of cell centers including 'ghost points' below the blade and branch cut at the trailing edge was generated by the codes. All data output in this research were values at cell centers. (See Figure 1) The blade geometry used for this research was the rounded trailing edge blade used by Driver and Beran as shown in Figure 2. (7)

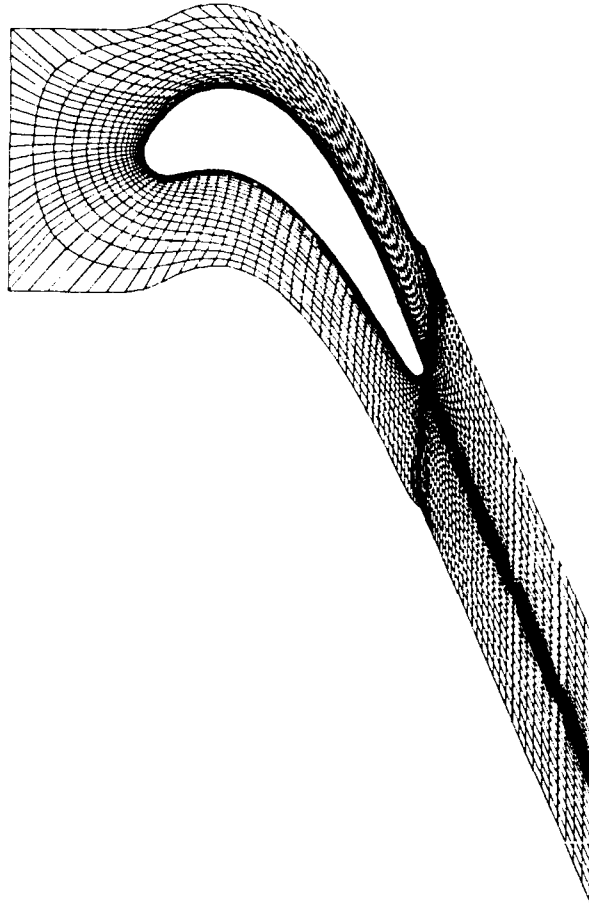


FIGURE 2: Grid for Rounded Trailing Edge Blade

#### II.4 Boundary Conditions (7:3-5)

Both codes used the same boundary conditions; although an additional boundary condition was incorporated to specify  $E_{vib}$  in ANTEC.

The subsonic inlet was assumed to be part of an imaginary duct extending infinitely far upstream. Disturbances in the computational domain are allowed to pass through the inlet, without reflection, and travel upstream as a simple wave. This assumption motivated the use of one-dimensional characteristic wave theory to establish boundary conditions at the inlet. One characteristic runs from the domain interior; therefore, only one quantity may be extrapolated while all others must be specified. The speed of sound was extrapolated while the

$M_2$  (inlet Mach),  $P_\infty$ , and  $T_\infty$  were specified. Once the speed of sound at the inlet,  $c_2$ , was determined,  $T_2$  was derived from the Riemann invariant

$$U_\infty + \frac{2}{(\gamma - 1)} c_\infty = U_2 + \frac{2}{(\gamma - 1)} c_2 \quad (46)$$

Far upstream the flow was at rest, and  $U_\infty$  vanishes. After a minor amount of manipulation, Equation 46 becomes

$$\frac{T_\infty}{T_2} = \left(1 + \frac{(\gamma - 1)}{2} M_2^2\right)^2 \quad (47)$$

Given  $M_2$  and  $T_\infty$ , the inlet temperature,  $T_2$ , can be solved for. Once this was known, the inlet pressure was easily obtained using the isentropic relationship

$$\frac{P_2}{P_\infty} = \left(\frac{T_2}{T_\infty}\right)^{\frac{\gamma}{\gamma - 1}} \quad (48)$$

The inlet vibrational energy necessary for ANTEC was also determined by  $T_2$  with the assumption that at steady state all waves will have passed back through the inlet, leaving the inlet in equilibrium.

Simple wave theory was again used to solve for the exit conditions. The flow was assumed to exit into a plenum that required the exit pressure,  $P_3$ , to match the plenum pressure; any pressure disturbances were reflected back into the computational domain. With the exit pressure specified, density at the exit was calculated using isentropic relationships

$$\rho_3 = \left( \frac{P_3}{S_{int}} \right)^{\frac{1}{\gamma}} \quad (49)$$

and

$$S_{int} = \left( \frac{P_{int}}{\rho_{int}} \right)^{\gamma} \quad (50)$$

Entropy, tangential velocity, and the Riemann invariant were extrapolated from the interior of the domain using one point and vibrational energy was extrapolated using two points.

For the C-grid used as shown in Figure 2, periodicity was applied along the outer boundary since the computational domain models one blade in an infinite cascade of blades. These periodic boundary conditions were applied at the ghost points located outside the computational domain. Along the wake cut, continuity was enforced.

On the blade surface, an adiabatic wall was assumed and normal-momentum was used to calculate pressure and velocities. To solve for the vibrational energy at the blade surface for ANTEC,  $E_{vib}$  was reflected. (4)

#### II.5 Initial Conditions (7:5)

The solutions for both ATEC and ANTEC were started at rest with the initial conditions for  $\rho$ ,  $P$ , and  $T$  in the computational domain being set to the constant values far upstream of the inlet. Due to the gas in the cavity starting at zero velocity with no discontinuities, equilibrium was assumed to exist initially to specify  $E_{vib}$  in ANTEC.

For this research, three cases were investigated and are summarized in Table 1:

1. a low-temperature, low-pressure case (as in reference 7)
2. the F100-PW inlet conditions and pressure ratio
3. increased inlet temperature with F100-PW pressure specifications.

In Cases 2 and 3,  $\gamma_a$  was adjusted based on the desired inlet temperature,  $T_2$ , and  $\gamma_a = 1.4$  for Case 1; even though at this low temperature, a corrected value of 1.3968 could have been used. (26:703-704) Decoupling of the vibrational energy results in a constant value  $\gamma_{ne}$  of 1.4 for ANTEC. This is based on the analysis of Liu and Vinokur. (15) They define a pressure derivative,  $\kappa$ , which is necessary in simplifying the nonequilibrium eigenstructure presented in the literature. (15,16) As electronic effects are excluded from this study,  $\kappa$  is defined only in terms of the translational/rotational value of  $c_v$  (Equation 17a); and nonequilibrium internal energies do not contribute to  $\kappa$ . (15:9) Therefore,  $\kappa$  is equal to  $2/5$  or  $\gamma_{ne} - 1$  when  $\gamma_{ne} = 1.4$ .

TABLE 1  
CASE SUMMARY FOR DESIRED INLET CONDITIONS

Case	$P_2$ (N/m <sup>2</sup> )	$T_2$ (°K)
1	$19.81 \times 10^4$	375.73
2	$215.81 \times 10^4$	1682.78
3	$215.81 \times 10^4$	2500.00

An inlet Mach number,  $M_2$ , was calculated with the following relationship:

$$\left(\frac{W}{W_{cr}}\right)^2 = \frac{(\gamma + 1)M_2^2}{2 + (\gamma - 1)M_2^2} \quad (51)$$

where the mean design  $W/W_{cr}$  for the blade is 0.317. (21)  $W/W_{cr}$  is the ratio of the relative gas velocity to the relative gas velocity corresponding to a Mach number of unity. Table 2 shows the values of  $\gamma$  for each case and the resultant  $M_2$ .

TABLE 2  
CASE SUMMARY FOR INLET MACH AND  $\gamma$

Case		$M_2$	$\gamma$
1	ATEC	0.352	1.4000
	ANTEC	0.352	1.4000
2	ATEC	0.297	1.3053
	ANTEC	0.292	1.4000
3	ATEC	0.298	1.2896
	ANTEC	0.292	1.4000

Using Equations 47 and 48, the values of  $T_{\infty}$  and  $P_{\infty}$  for Cases 2 and 3 were obtained using desired inlet conditions. The appropriate values of  $M_2$  and  $\gamma$  are shown in Table 2. The values for  $T_{\infty}$  and  $P_{\infty}$  used in Case 1 were calculated by Driver and Beran and given to the author as a test case. Using  $W/W_{cr} = .381$  as in reference 7, values of  $M_2$ ,  $T_2$  and  $P_2$  for Case 1 were calculated using Equations 47, 48, 51 and the gas tables in reference 26. The value of  $T_2$  used in Case 3 was 2500°K. The pressure ratio,  $P_2/P_3$ , was calculated to be 3.11 for Case 1 and the F100

pressure ratio used was 3.66. Since the values of  $\gamma_{re}$  and  $M_2$  for ANTEC do not change for Cases 2 and 3, the ratio,  $T_2/T_{\infty}$ , was constant. Therefore,  $P_{\infty}/P_2$  was also constant. Emphasis was placed on matching the inlet conditions between the two version so that accurate comparisons could be made and appropriate conclusions drawn. The conditions calculated far upstream are summarized in Table 3.

TABLE 3  
CASE SUMMARY FOR CONDITIONS FAR UPSTREAM

Case		$P_{\infty}$ (N/m <sup>2</sup> )	$T_{\infty}$ (°K)
1	ATEC	$29.31 \times 10^4$	420.16
	ANTEC	$29.31 \times 10^4$	420.16
2	ATEC	$312.57 \times 10^4$	1835.07
	ANTEC	$320.24 \times 10^4$	1883.64
3	ATEC	$311.30 \times 10^4$	2714.37
	ANTEC	$320.24 \times 10^4$	2798.41

### III. Results

A brief discussion of the shock tube results can be found in Appendix A. This section will focus on the comparative results obtained with ANTEC and ATEC.

#### III.1 Case Summary

The cases discussed in Section II.5 were investigated at steady-state, since reasonable comparisons could only be made between steady-state solutions. Once attained, the flow parameters could then be evaluated. Of particular interest were the flow temperatures along the blade, in the vicinity of the shock and the trailing edge.

Table 4 shows the steady-state values attained for each case and the percentage difference from the desired inlet values. Both versions did poorly compared to the calculated  $M_2$  in Table 2. The results were closer to the F100 turbine inlet Mach number of 0.4.  $M_2$  is driven by the pressure ratio; or if the flow is choked, it will be determined by the area ratio of the inlet duct and the passage. The design pressure ratio for the blade is 2.239 (21), which is lower than the pressure ratios used in this study.

TABLE 4  
COMPARISONS TO DESIRED INLET CONDITIONS

Case	$P_2$ (N/m <sup>2</sup> )	% Dif	$T_2$ (°K)	% Dif	$M_2$	% Dif	
1	Desired	$19.81 \times 10^4$		375.73		.352	
	ATEC	$20.11 \times 10^4$	1.51	374.68	0.28	.364	3.4
	ANTEC	$19.61 \times 10^4$	1.01	374.56	0.31	.366	4.0
2	Desired	$215.81 \times 10^4$		1682.78		.297* .292**	
	ATEC	$215.19 \times 10^4$	0.29	1681.21	0.09	.370	27.59
	ANTEC	$215.59 \times 10^4$	0.10	1682.27	0.03	.358	23.45
3	Desired	$215.81 \times 10^4$		2500.00		.298* .292**	
	ATEC	$215.53 \times 10^4$	0.13	2499.26	0.03	.370	27.59
	ANTEC	$215.83 \times 10^4$	0.01	2500.07	.003	.357	23.10

\* ATEC value

\*\* ATEC value

A trial case of ANTEC was run using  $M_2 = .4$  to calculate the necessary input values of  $T_{in}$  and  $P_{in}$ . For this case, the flow was choked through the passage and the inlet values do not drop to the desired F100 values. If this case had been investigated further, choked flow should not present a problem for this particular study. If matching inflow conditions were obtained from ATEC, a valid comparison would still be possible. Driver and Beran have found in their research, using the rounded trailing edge blade, that  $M_2$  has an asymptotic upper limit of .367 at a pressure ratio of 3.239. (7:13)

The percentage difference is presented in Table 4 as a point of interest. What the author finds curious was how the numerically

calculated inlet pressures and temperatures equal the analytical values. The desired inlet conditions were based on the values of  $M_2$  in Table 2, and the values of  $M_2$  generated by the codes are significantly different. Since emphasis was placed on matching inflow conditions, the difference between the values of  $M_2$  was not considered a problem. If further work is done on this subject, the F100 pressure ratio and inlet pressure could be replaced by blade design data. (21) Alternately, the blade could be replaced with the F100 blade geometry. Eliminating the mixing of geometries and conflicting parameters should isolate or eliminate this curiosity.

### III.2 CFL Criteria and Convergence Histories

The Courant-Friedrichs-Lewy (CFL) condition is a stability requirement where  $v$ , called the Courant number, is defined by

$$v \equiv c \Delta_t / \Delta_x \quad (52)$$

(1:75)

All ANTEC cases used a CFL value of .95. However to successfully run ANTEC for Cases 1 and 3, the time step had to be adjusted after a number of iterations. Following start up, ANTEC Case 1 yielded a satisfactory transient solution until at a certain time ( $t \approx .047$  seconds) the numerical solution became undefined, thus making the time step suspect. (5) Therefore, the cases were then run in intervals of iterations, as demonstrated in Table 5. If the solution became undefined in an interval, the CFL number was decreased and the code was restarted (see Appendix C for a discussion on the RESTART file). After

adjusting the CFL number, the code again would progress. Once the solution was approaching steady-state, the CFL criteria could again be raised. A similar problem was encountered by Driver and Beran in their research in the test cases where the contact surface was in the vicinity of the trailing edge. (7:15) For this reason, it was originally assumed that the numerical solution for ANTEC became undefined at the trailing edge. However, investigation of the flow showed that the problem was at the inlet. Figure 3 shows the region at the inlet where the solution becomes undefined. Since this problem was only seen in ANTEC and not ATEC, the inlet boundary condition for vibrational energy was suspected as being the cause.

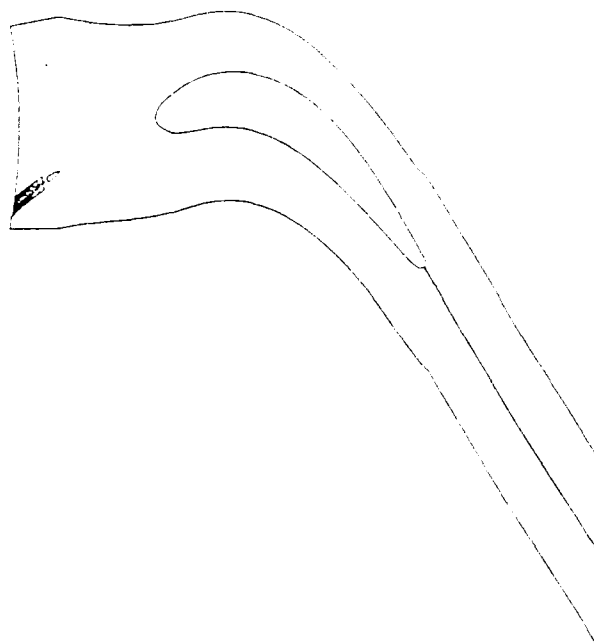


Figure 3: Region of Undefined Solution

Table 5 summarizes the progression of CFL numbers for the different cases. An additional high-temperature case is listed as a point of interest. Case 3 was never run at an initial CFL value of .95

due to an intermediate case with  $T_2 = 2000^\circ\text{K}$  having problems after 1000 iterations at .95. Therefore, it is not known if Case 3 could be started at a higher CFL number and then be adjusted as with Case 1.

TABLE 5  
CFL CHANGES

Case	Number of iterations	CFL
1	1-3500	.95
	3501-4500	.90
	4501-8000	.95
2	1-8000	.95
3	1-9000	.90
	9001-10000	.95
$T_2=3000$	1-1000	.60
	1001-4000	.50
	4001-7000	.60
	7001-9000	.70

To determine if steady-state had been reached, the convergence history for each case was recorded. These histories are shown in Figures 4-9; with the convergence being determined by the norm calculated as

$$N(U) = 100 \{ \max [ \text{abs}(1 - U_k^n / U_k^{n+1}) ] \} \quad (53)$$

which gave a percentage difference between the present and previous solutions at each point with the final norm value being the maximum

difference in the grid. Therefore, if just one point continually fluctuated due to a numerical or physical phenomena, the convergence history may appear not to reach a steady state as seen in ANTEC Case 3, Figure 9. Had the nonequilibrium Case 2, Figure 7, been run for as many iterations, it may have exhibited similar behavior. These oscillations are consistent with Driver and Beran's results for the rounded trailing edge blade used in this study. (7:10)

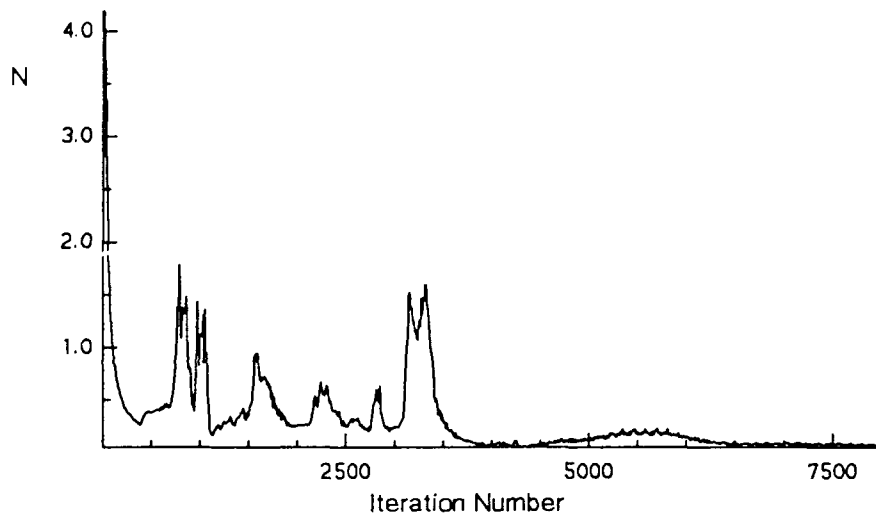


Figure 4: Convergence History for ATEC (Case 1)

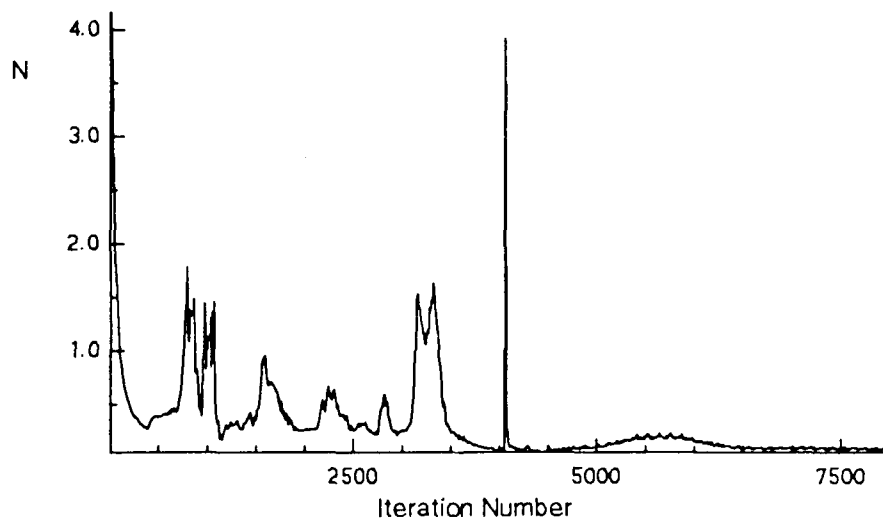


Figure 5: Convergence History for ANTEC (Case 1)

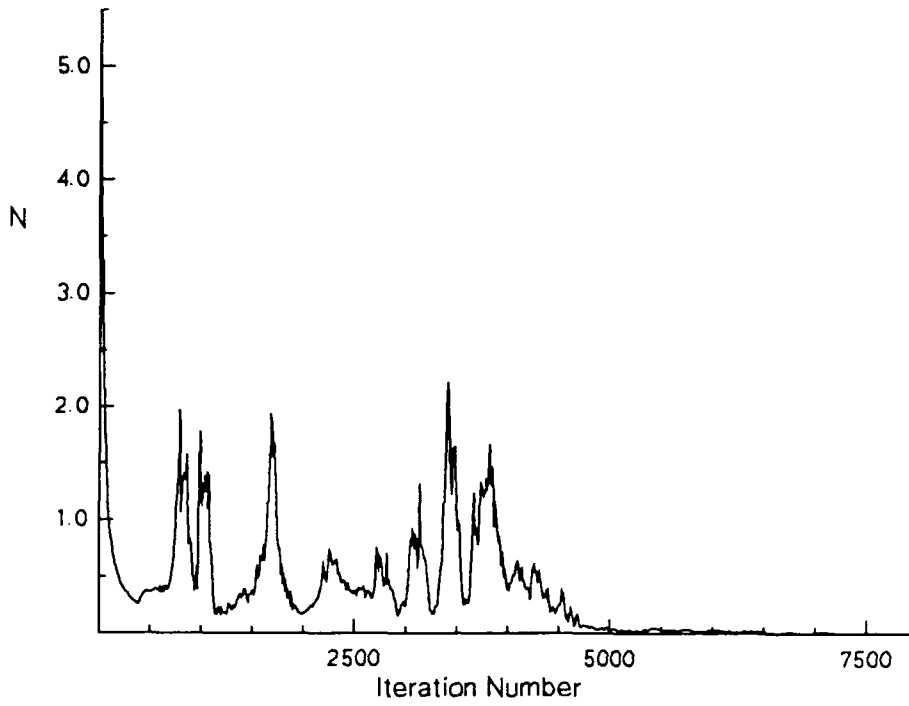


Figure 6: Convergence History for ATEC (Case 2)

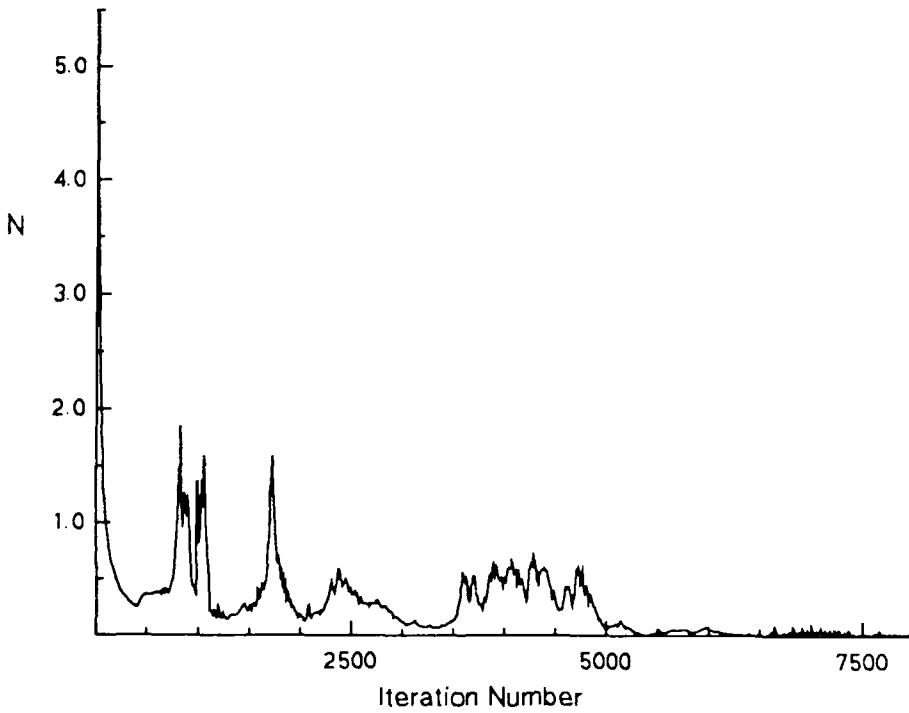


Figure 7: Convergence History for ANTEC (Case 2)

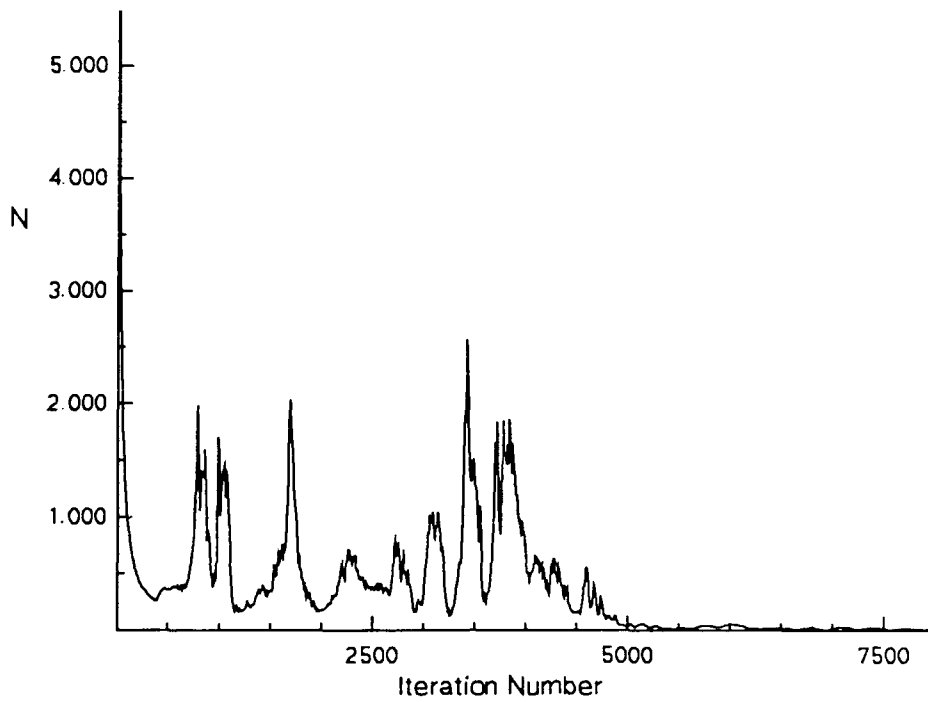


Figure 8: Convergence History for ATEC (Case 3)

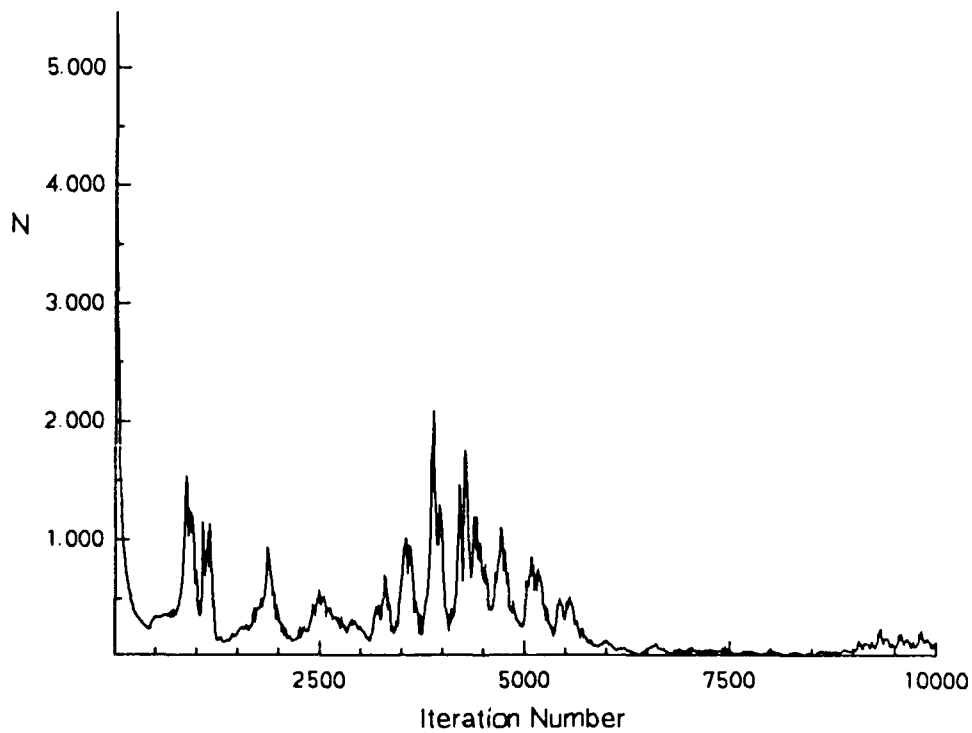


Figure 9: Convergence History for ANTEC (Case 3)

Except for a spike in the ANTEC results, both codes had identical convergence histories for Case 1 (Figures 4 and 5). For Cases 2 and 3, the norms from ATEC reached a 'smoother' steady-state solution than those from ANTEC (Figures 6-9). In Figure 9, the oscillations appear to begin where the CFL was raised to .95. However, there is no such correlation between CFL and the norms in Figure 5. Therefore, more test cases would have to be run before an assertion of a connection between CFL number and solution oscillations was made.

### III.3 Blade Temperature Profiles

The trends observed for the comparisons of the blade temperature profiles did not correspond to those of a blunt-nosed body in hypersonic flight as previously mentioned in Section I.1. However, for the flow conditions present, the results were realistic.

Figures 10-12 are the blade temperature profiles for the three cases investigated. The stagnation temperature on the lower blade surface, known as the pressure surface, was as expected and corresponded closely to the inlet temperature. For Case 2, the results from ANTEC show the stagnation temperature was 1673.19°K, or 0.54% different than the inlet temperature; and for Case 3, it was 2484.37°K, 0.63% different (Figures 11 and 12).

At the blade tip, there was a very close correspondence between the blade temperatures predicted by the two codes, which was also expected. This part of the blade was in equilibrium as shown by the overlapping of the blade temperature and  $T_{vb}$  from ANTEC. Here, the

internal energies of the flow produced by the two codes were equal. With  $e_{int}$  defined as

$$e_{int} = c_v T \quad (54)$$

the following relationship was observed

$$(c_v T)_{ne} = (c_v T)_a \quad (55)$$

For Cases 2 and 3, as the flow moved from this reference point, expanding and cooling over the upper (or suction) surface, the temperature decrease behaved differently for the two codes based on the values of  $\gamma_{eff}$  and  $\gamma_a$ .  $\gamma_{eff/a}$  (Equation 14) can also be defined as

$$\gamma_{eff/a} = 1 + \frac{R}{c_v} \quad (55)$$

With  $\gamma_a$  and  $R$  constant,  $c_v$  must also be constant (a calorically perfect gas). In ANTEC, neither  $\gamma_{eff}$  nor  $c_v$  can be assumed constant, but were temperature dependent as demonstrated in Equations 14-17. The value of  $c_v$  denotes the capacity of the gas to hold energy. As the temperature decreased, ANTEC retained the same capacity to store energy. However, in the nonequilibrium version,  $\gamma_{eff}$  was increasing due to  $c_v$  decreasing; capacity to store energy was lost, resulting in higher temperatures.

Another way to look at this is to assume the flows in both code versions were transferring internal energy to kinetic energy at the same rate along the blade, retaining internal energies that were approximately equal to each other. At any arbitrary point along the blade  $(c_v T)_{ne} = (c_v T)_a$ . Again observing the suction surface, the value of  $c_{v_a}$  was constant, but  $c_{v_{ne}}$  had decreased due to the cooling in the

expansion. Clearly for the energies to be equal,  $T_{ne}$  must be greater than  $T_a$ .

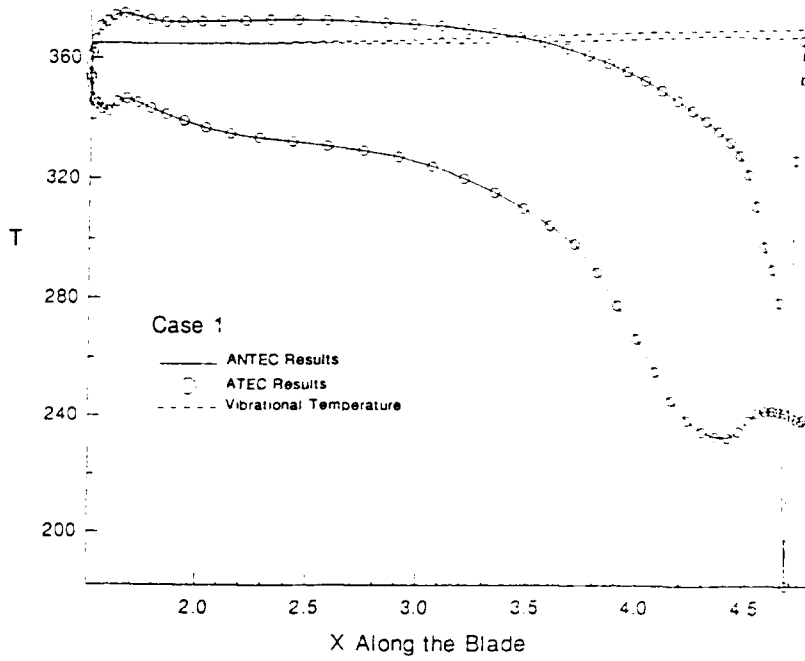


Figure 10: Blade Temperature Profile Case 1

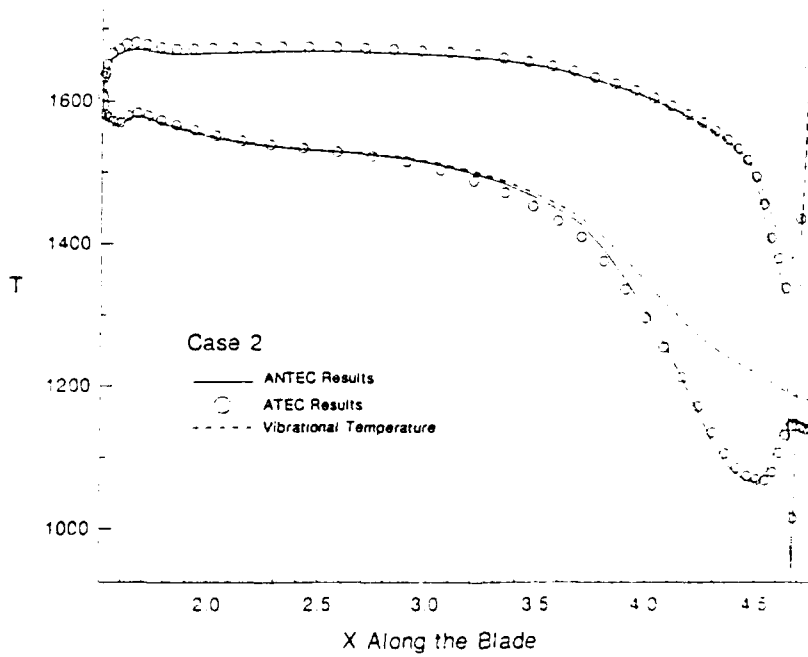


Figure 11: Blade Temperature Profile Case 2

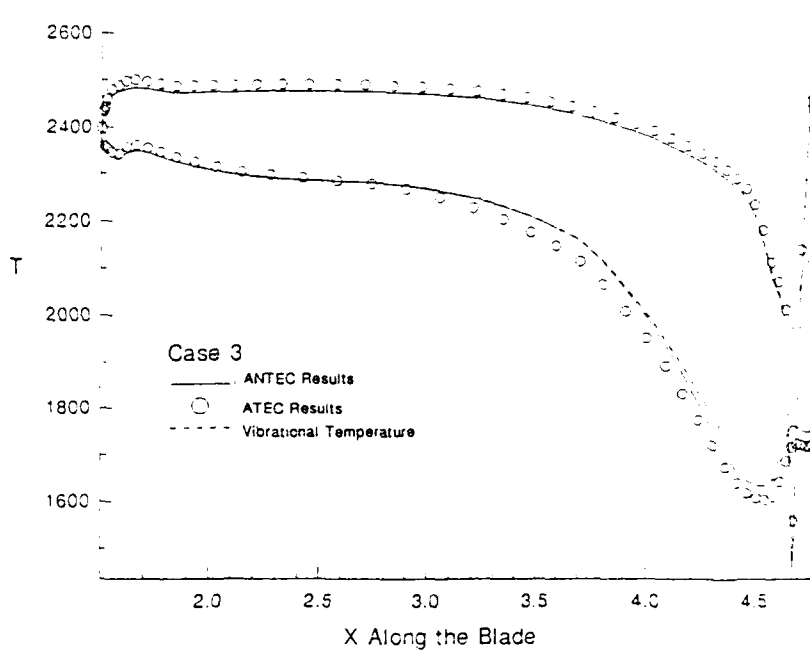


Figure 12: Blade Temperature Profile Case 3

The blade temperatures for the two methods at the low-temperature case were as expected, very close to equal. However, the low-temperature case posed a problem to the nonequilibrium model. The characteristic time of the problem,  $\Delta_t$ , was smaller than the relaxation time,  $\tau$ . Physically, for a cold, low-pressure flow, relaxation will be relatively long. For this case, at 8000 iterations,  $\Delta_t$  was on the order of  $10^{-6}$  and  $\tau$  was on the order of  $10^{-4}$ . Therefore, the flow had not reached equilibrium. Clearly, the solution would be to employ local time stepping. By Equation 8, as temperature increases,  $\tau$  will decrease. Since  $\tau$  for Case 2 was on the order of  $10^{-10}$ , no time scale problem existed for the high-temperature cases and the nonequilibrium model was able to reach a physical solution.

#### III.4 Trailing Edge Temperatures

After studying the overall blade temperature profile, the trailing edge was of particular interest due to the complex flow structure in this area.

On the pressure surface, the temperature was relatively constant until the trailing edge (Figures 10-12). These blade profiles showed a rapid expansion and decrease in temperature followed by an immediate compression or shock. The suction surface also had a rapid compression at the trailing edge. The changes in temperature before this compression were due to the blade and cascade geometry. The shock created at the trailing edge of the pressure surface was impacting the suction surface, causing a slight compression. An expansion was caused by the rounded trailing edge. The rapid compressions experienced by both surfaces were in order to meet the Kutta condition, which states that pressures from the suction and pressure surfaces must be equal at the trailing edge stagnation point.

Figures 13 and 14 highlight the trailing edge geometry and show the differences between the two code versions in the vicinity of the trailing edge for Case 3. For this case, the maximum temperature differences over the entire grid were  $-741^{\circ}\text{K}$  and  $539^{\circ}\text{K}$ . These were at the trailing edge as demonstrated by the extreme light and dark shaded regions in Figure 13 and were not evident on the blade. Although weakened, Figure 14 also demonstrates the pressure surface trailing edge shock impacting the suction surface. The shape of the trailing edge appears different in these figures due to the different scalings.

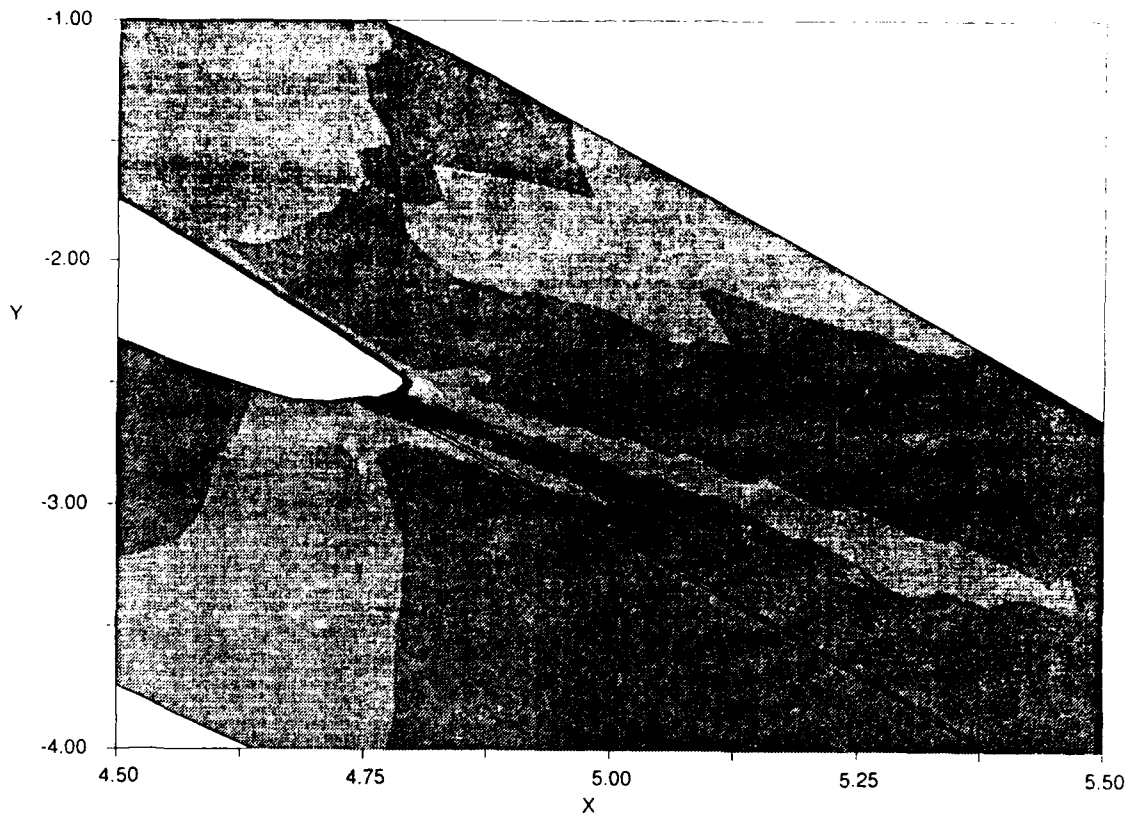


Figure 13: Expanded View of Temperature Differences at the Trailing Edge  
Case 3

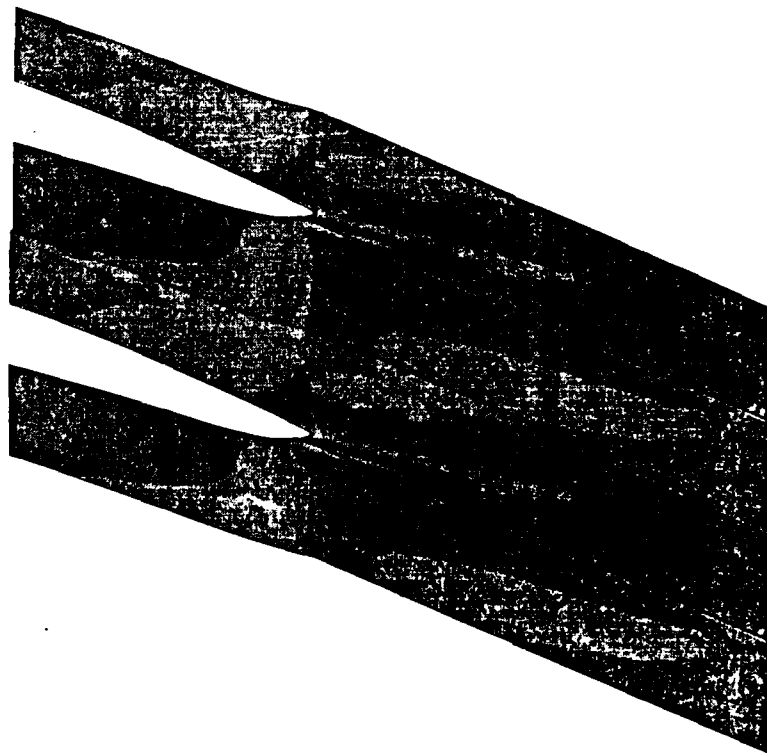


Figure 14: Expanded View Showing Shock Impact on Suction Surface  
Case 3

### III.5 Gamma Comparisons

Figures 16 and 17 show how *gradually*  $\gamma_{\text{eff}}$  changes along the blade (at the ghost points) with temperature, and it can be seen that the value of  $\gamma_{\text{eff}}$  everywhere on the blade was higher than  $\gamma_a$ . Therefore, even through the shock, where temperatures sharply increase, the increase was not enough to significantly increase the capacity,  $c_v$ , of the nonequilibrium flow and cause lower temperatures than those predicted by ANTEC.

Again, the low-temperature case (Case 1) showed difficulty due to the flow not being able to reach equilibrium. An accurate value of  $\gamma_{\text{eff}}$  could not be calculated. The expected trend as the flow expanded would be for  $\gamma_{\text{eff}}$  to approach 1.4. Figure 15 shows this is not the case.

The blade profiles of  $\gamma_{\text{eff}}$  for all cases closely resembles the  $T_{\text{vib}}$  curves in Figures 10-12, but inverted. For ease of comparison, Figure 18 is the vibrational temperature for Case 3. In ANTEC,  $T_{\text{vib}}$  is extracted from  $e_{\text{vib}}$  (Equation 7) and  $e_{\text{vib}}$  is dependant on  $c_{\text{vib}}$  (Equation 53). Knowing the dependence of  $\gamma_{\text{eff}}$  on  $c_{\text{vib}}$ , a relationship between  $\gamma_{\text{eff}}$  and  $T_{\text{vib}}$  can be deduced showing that as  $\gamma_{\text{eff}}$  increases,  $T_{\text{vib}}$  decreases. This trend is indeed shown between  $T_{\text{vib}}$  and  $\gamma_{\text{eff}}$  on the blade, Figures 17 and 18. The decoupling of vibrational energy does indeed 'correct' the value of  $\gamma_{\text{eff}}$  from 1.4 to an appropriate value for the flow.

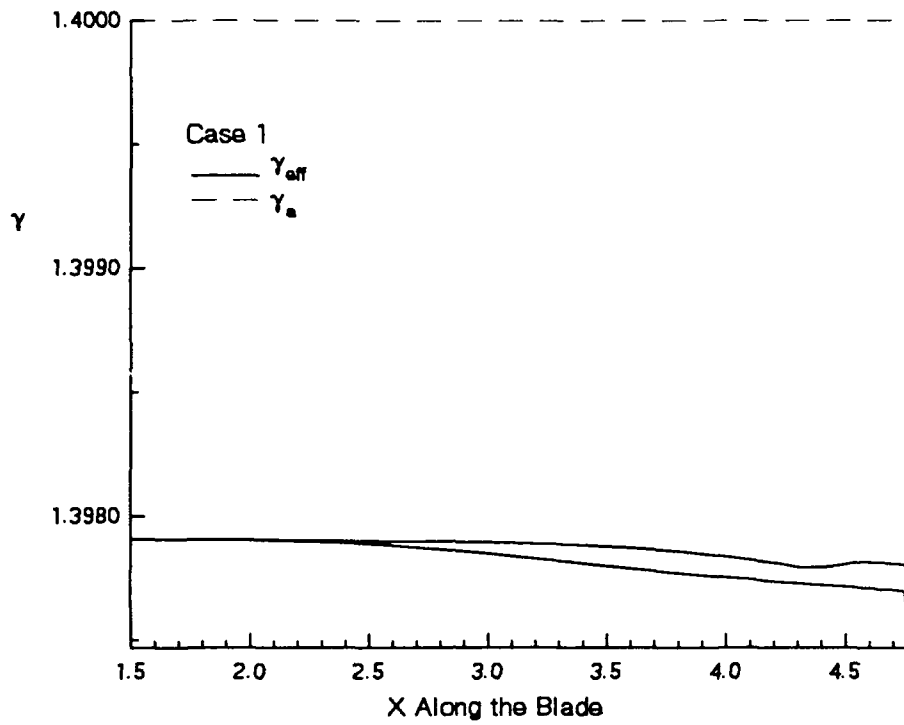


Figure 15: Gamma Comparison for Case 1

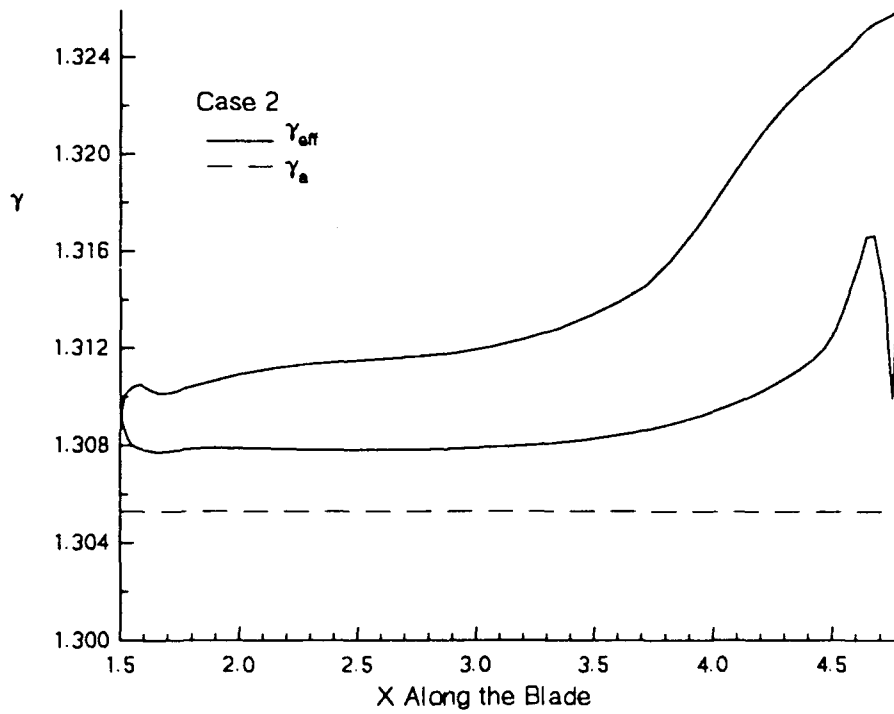


Figure 16: Gamma Comparison for Case 2

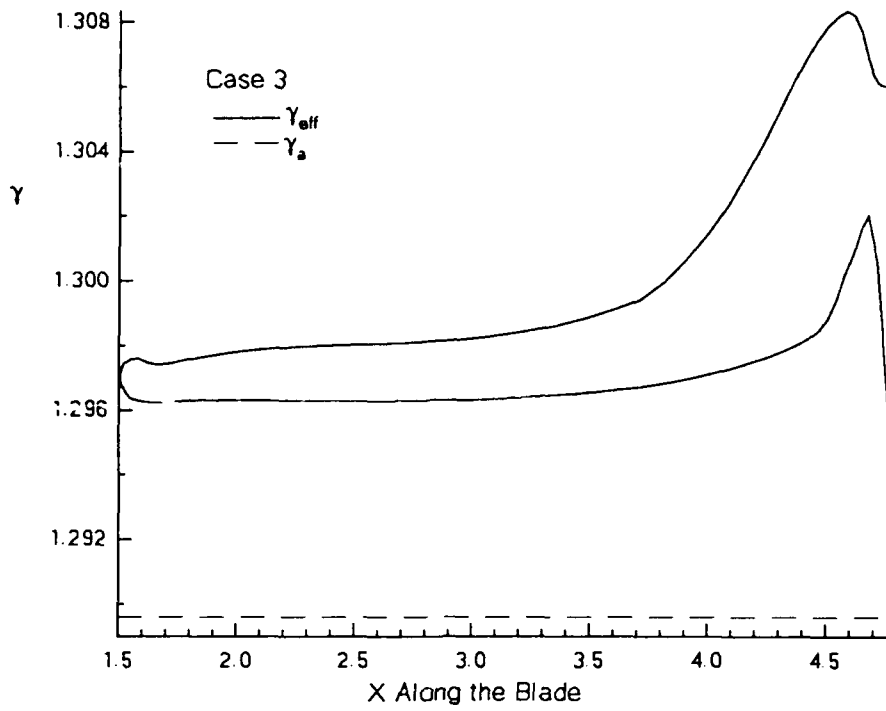


Figure 17: Gamma comparison for Case 3

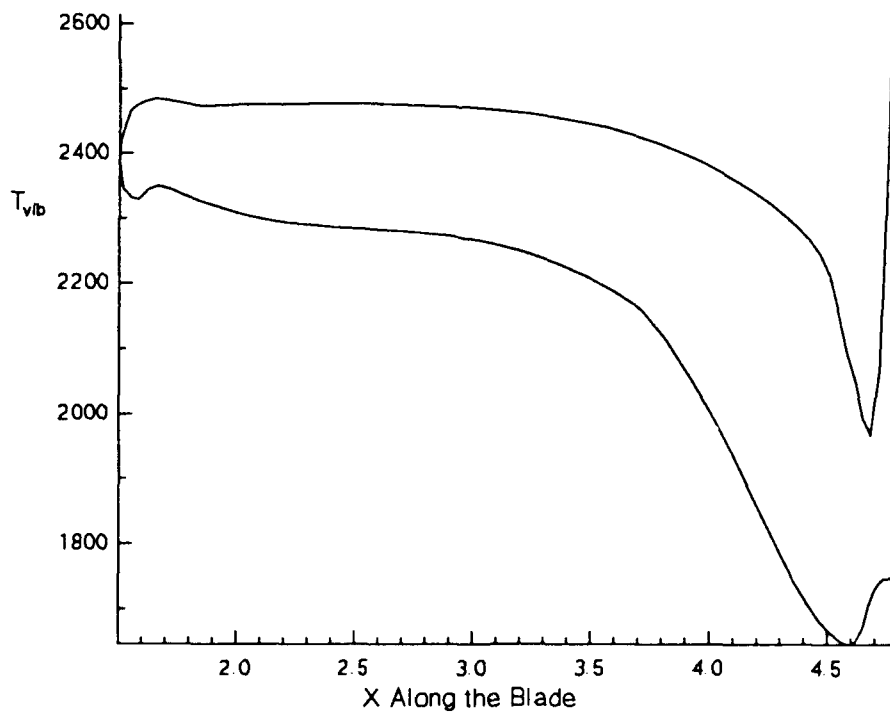


Figure 18: Vibrational Temperature for Case 3

### III.6 Computational Time Comparisons

As important as accurate models are, there is usually a penalty paid with increased CPU time. Most of the runs for the cases investigated were run in the "background" system mode. Although an efficient way to run a large job, 1000 iterations could take anywhere from 1 to 2 1/2 hours to complete, depending on system usage.

ATEC, and hence its modification, ANTEC, were optimized to run on a CRAY-XMP; however, all computations for this effort were performed on Stardent ST2000. Therefore parallelization on the Stardent was not an efficient use of the processors and the runs were completed using vectorization only.

TABLE 6  
COMPUTER TIME COMPARISONS  
CPU SECONDS/ITERATION

Version	No Optimize	Vectorize	Vectorize and Parallelize
ATEC	7.53	0.84	1.99
ANTEC	11.79	1.36	5.93

Interactive runs were made to compare the run times of ATEC with those of ANTEC at different levels of optimizations. Table 6 summarizes the average CPU time per iteration for the two versions. Both were compiled and run using: 1. no optimization; 2. vectorization only; and 3. parallelization and vectorization. With no optimization, the codes were only run for 100 iterations. The codes compiled this way were

never used to arrive at a steady-state solution of the gasdynamic equations. The other test runs were performed with 1000 iterations and are more representative of actual 'runs.' The time required to output the data files after completion of the iterations can be considered constant; therefore, these average times per iteration should decrease slightly as the number of iterations is increased.

## IV. Conclusions and Recommendations

### IV.1 Conclusions

This comparative study between ATEC, a two-dimensional, explicit Euler code, and a version modified to account for vibrational energy, ANTEC, has shown the impact of  $\gamma$  in computing transonic flow through a turbine cascade. The assumption of a calorically perfect gas may simplify the computations; however, even when corrected for high temperatures, a constant value of  $\gamma$  for the entire flowfield is inaccurate. It was the purpose of this investigation to determine the limitations of the assumptions and the models. For Case 3, the extreme temperature differences were  $-741^{\circ}\text{K}$  and  $539^{\circ}\text{K}$  and were located at the trailing edge. These values may not appear as significant as the  $5,100^{\circ}\text{K}$  temperature difference for the hypersonic blunt-nose body mentioned in Section I.1; however, such extreme differences were not anticipated.

The use of ANTEC for the high-temperature cases resulted in higher blade temperatures over the suction surface. With steady, equilibrium inflow conditions, the tip of the blade was also in equilibrium as demonstrated by  $T = T_{\text{vib}}$  in this area. Areas of nonequilibrium were seen toward the trailing edge on the suction surface and at the trailing edge.

Even at low temperatures, where the nonequilibrium model showed difficulty due to a large relaxation time, there were small differences. However, these differences could be considered minor depending on the

accuracy of the estimation desired. Having based the algorithm of the Euler equations, other important aspects of transonic flow through a turbine cascade such as heat transfer are ignored, making the code a tool for estimation. Incorporation of the thermal nonequilibrium model allows the designer to simulate higher temperature flows with a greatly improved level of accuracy.

#### IV.2 Recommendations for Further Study

1. Eliminate the mixture of blade and design parameters and vary the inlet temperatures. This would possibly identify any peculiarities in this investigation caused by using F100 inlet parameters with the NASA test blade geometry.

2. Modify ANTEC to use a steady-state ATEC RESTART file as the initial conditions to help alleviate the computer time required for the nonequilibrium model.

3. Incorporate the nonequilibrium model without the assumption of air being a single species.

4. Conduct a parametric study varying input parameters discussed in Appendix C that were held constant for this investigation.

5. To simulate equilibrium flows, modify ATEC to have a 'look-up' table for  $\gamma_a$  and compare the results and computer times with the nonequilibrium version.

## Appendix A: Shock Tube Analysis

To gain an understanding of second-order accurate shock capturing schemes and the nonequilibrium model, unsteady flow in a shock tube was investigated. The shock tube is a valuable learning tool since an analytic solution can be found and much is available in the literature exists for comparisons.

Gas in the left side of the tube was initially set to high pressure and density with the other side being of lower pressure and density. Ideally, a shock should be captured by no more than one node, since this would more closely model the instantaneous changes caused by a shock. Therefore, capturing the shock with a minimal number of nodes is desirable. Also, a shock tube not only has the shock discontinuity, but changes in flow parameters due to the contact surface and expansion fan as well.

A comparison of the nonequilibrium code versus an ideal gas code was made (Figure 19). The nonequilibrium results nearly match those reported by Moran. (16,17)

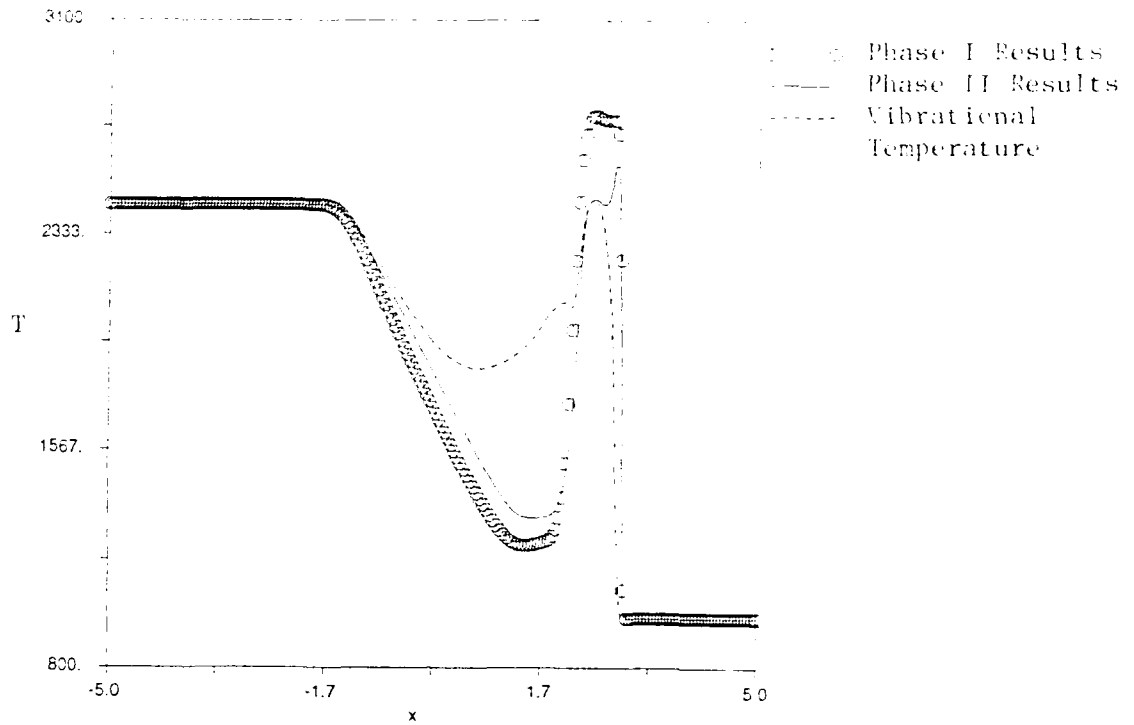


FIGURE 19: Shock Tube Results

The TVD scheme used in Phases One and Two was different from the one applied in ATEC. The shock tube used Harten's ULT1C. (12) The differences between the two schemes are now described.

There is no change to the form of the finite difference scheme or numerical flux (equation numbers are repeated for identical formulas)

$$U_j^{n+1} = U_j^n - \lambda (\bar{f}_{j+1/2}^n - \bar{f}_{j-1/2}^n) + \Delta_t S \quad (32)$$

$$\bar{f}_{j+1/2} = \frac{1}{2} \left[ F(U_j) + F(U_{j+1}) + \frac{1}{\lambda} \sum_{k=1}^m R_{j+1/2}^k \beta_{j+1/2} \right] \quad (33)$$

$R_{j+1/2}^k$  is still the eigenvector matrix (Equation 22) but the effective numerical viscosity,  $\beta_{j+1/2}$ , is defined as

$$\beta_{j+1/2} = (\tilde{g}_j + \tilde{g}_{j+1}) - Q(v_2^k) \alpha_{j+1/2}^k \quad (57)$$

with the same values of  $v$ ,  $\alpha_{j+1/2}^k$ , and  $Q$

$$v_2^k = \lambda a_{j+1/2}^k + \gamma_{j+1/2}^k \quad (35)$$

$$v_1^k = \lambda a_{j+1/2}^k \quad (36)$$

$$\alpha_{j+1/2}^k = \left[ R_{j+1/2}^k \right]^{-1} \Delta_{j+1/2} U \quad (37)$$

$$\Delta_{j+1/2} U = U_{j+1} - U_j \quad (38)$$

$$Q(z) = \frac{z^2}{4\epsilon} + \epsilon \quad \text{for } |z| < 2\epsilon \quad (40)$$

$$Q(z) = |z| \quad \text{for } |z| \geq 2\epsilon$$

but  $\sigma$  becomes

$$\sigma_{j+1/2}^k(z) = \frac{1}{2} (1 - Q(z)) \quad (58)$$

$\epsilon$  is still an input parameter. In the shock tube code a value of 1/2 was used due to lesser values causing an undefined solution (a value of 0 was used in both ATEC and ANTEC). This sensitivity was also seen by Moran. (16)

The linearly degenerate fields,  $a^k = u$ , are described first.  $\tilde{g}_j^k$  is determined from

$$\tilde{g}_j^k = \bar{g}_j^k + \theta_j \bar{\bar{g}}_j^k \quad (59)$$

$$\bar{g}_j^k = s_{j+1/2}^k \max[0, \min(|\bar{\bar{g}}_{j+1/2}^k|, \bar{\bar{g}}_{j-1/2}^k s_{j+1/2}^k)] \quad (60)$$

$$\bar{\bar{g}}_j^k = S_{j+1/2}^k \max[0, \min(S_{j+1/2}^k \sigma_{j-1/2} \alpha_{j-1/2}, c_{j+1/2} |\alpha_{j-1/2}|)] \quad (61)$$

$$\bar{\bar{g}}_{j+1/2}^k = \frac{1}{2}[Q(v_1^k) - (v_1^k)^2] \alpha_{j+1/2}^k \quad (62)$$

with

$$s_{j+1/2}^k = \text{sign}(1, \alpha_{j+1/2}^k) \quad (42)$$

$$S_{j+1/2}^k = \text{sign}(1, \bar{\bar{g}}_{j+1/2}^k) \quad (63)$$

where 'sign' operator assigns the sign (+ or -) of the second value in parenthesis to the first value.  $\theta_j$  is defined by

$$\theta_j = \frac{|\alpha_{j+1/2}^k - \alpha_{j-1/2}^k|}{|\alpha_{j+1/2}^k| + |\alpha_{j-1/2}^k|} \quad (64)$$

Now the treatment of the nonlinear fields,  $\mathbf{a}^k = \mathbf{u} \pm \mathbf{c}$ , is described.  $\tilde{g}_j^k$  is determined from

$$\tilde{g}_j^k = \bar{g}_j^k \quad (65)$$

$\gamma_{j+1/2}^k$  is unchanged from the Harten-Yee formulation used in ATEC and ANTEC

$$\gamma_{j+1/2}^k = \sigma(v_{j+1/2}^k) \frac{(\tilde{g}_{j+1/2}^k - \tilde{g}_{j-1/2}^k)}{\alpha_{j+1/2}^k} \quad \text{for } \alpha_{j+1/2}^k \neq 0 \quad (44a)$$

$$\gamma_{j+1/2}^k = 0 \quad \text{for } \alpha_{j+1/2}^k = 0 \quad (44b)$$

The values to be used for the eigenvalues and eigenvector matrices for the equilibrium code (Phase One) can be found in references 4 and 12, and in references 15, 16 and 17 for the nonequilibrium code (Phase Two).

## Appendix B: Code Modification

Due to the modularity of ATEC, incorporation of the nonequilibrium model into ATEC was very straightforward. The largest task was changing the Jacobian matrices and their inverses to account for the added vibrational energy equation; systems of 4x4 matrices were extended to systems to 5x5 matrices.

Along with  $\rho$ ,  $\rho u$ ,  $\rho v$  and  $E_T$ , the vibrational energy had to be calculated at cell centers, and Roe averaged at cell interfaces. From  $e_{vib}$ ,  $T_{vib}$  could be calculated using Equation 7.  $T_{vib}$  was not necessary to obtain a steady-state solution, but it was necessary to determine whether or not the solution was in equilibrium once steady state was attained.

Calculation and application of the source term was the significant difference between ANTEC and ATEC. Therefore, Equations 2, 6, 8, 9, 10, and 13 were incorporated into ANTEC along with the modified equations for pressure, total energy and speed of sound (Equations 12, 3, and 28).

To verify proper implementation of the nonequilibrium model, the modified version was run with the source term set to zero (conservation of vibrational energy) and results were identical to those of the unmodified version as seen in Figure 20.

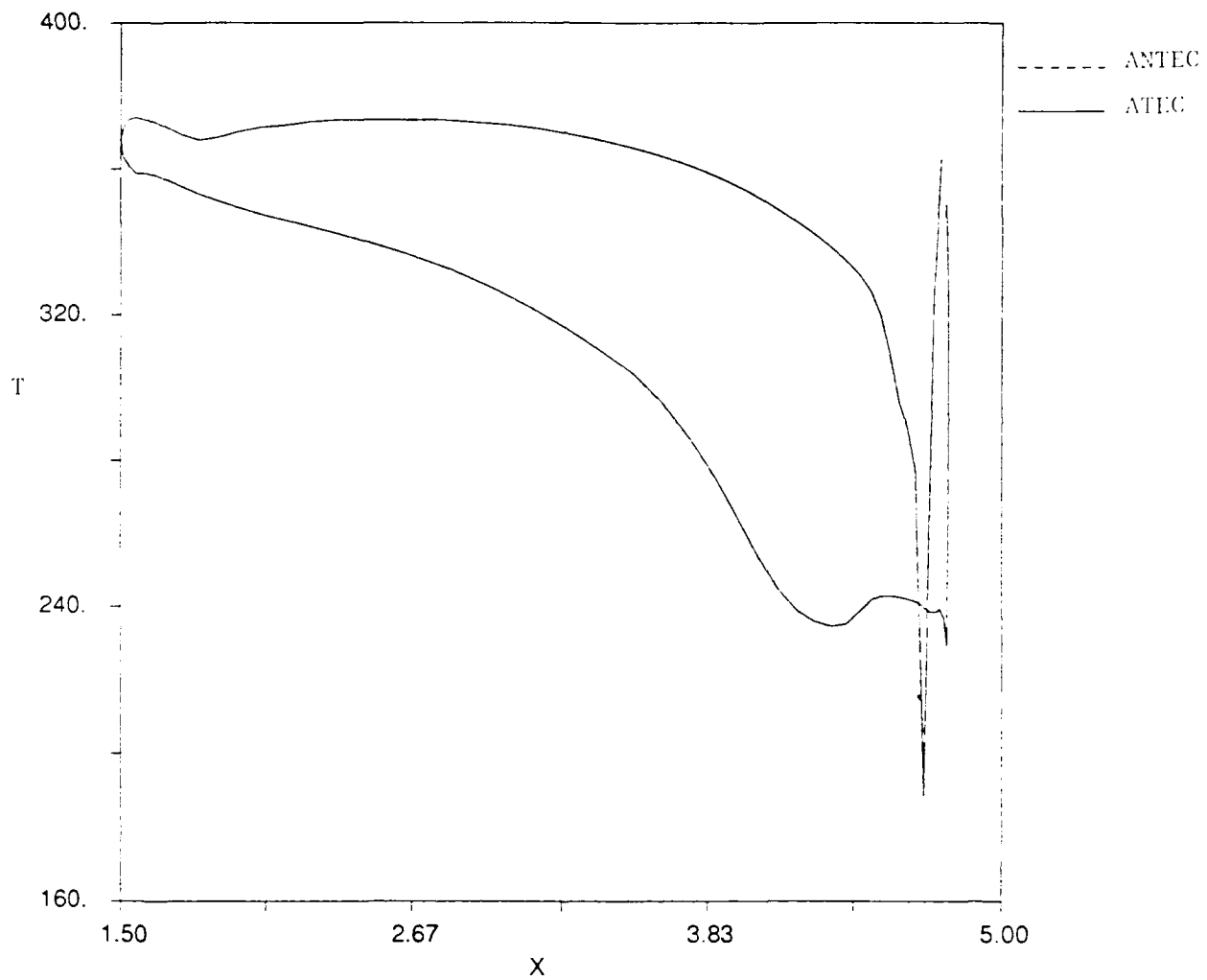


FIGURE 20: Conservation of Vibrational Energy

### Appendix C: Code Input

ATEC and ANTEC are general codes written to run for a variety of flow conditions and grid sizes, as delineated in the CASIN file.

This file first defines  $P_{in}$  and  $T_{in}$ . These are derived using Equations 47 and 48. To obtain an accurate comparison between ATEC and ANTEC, it was important to match the inlet conditions for each test case.

Next CASIN, lists the flow angle. This parameter was not altered for any of the cases.

The plenum pressure, obtained from calculations based on the desired inlet pressure and stage pressure ratio, is then input.

The following two fields are used to start the codes running from zero or to use a RESTART file and determine how many iterations to run. If a 1 is entered, the computational domain will be initialized and computations will begin. If any number other than 1 is listed, a RESTART file will be used. The number of iterations specified will be run and the U vector for all grid points will be written to RESTART. With the restart capability, the code can be stopped, the development of the flow field can be examined, and then the code can be started again. This feature is also convenient when a steady-state solution is desired, yet how many iterations are necessary to reach this condition is not known. If, for example, 5000 iterations are accomplished and the code is stopped and the solution is not yet at steady-state; then the CASIN

is easily edited for more iterations using the solution at 5000. Without the restart capability, much computer time would be wasted.

Next, the CFL condition is input. For ATEC this was always .95. However, this parameter had to be adjusted for ANTEC which was discussed in Section III.2.

The code can run either a first order or second order solution. With an input value of 1, the code will run a first order Roe scheme; with a value of 2, the code will run the second order TVD scheme based on ULT1C. The value 2 was always used in this investigation.

The next seven fields deal with the grid by defining the maximum number of nodes in each direction, the location of the diaphragm, and the positions of the blade trailing edge and the periodic boundaries. These parameters were never varied.

As mentioned in the section dealing with the development of the TVD scheme,  $\epsilon$  and  $\omega$  are input parameters. These also were never varied. The value of  $\epsilon$  was zero for both the linearly degenerate and genuinely nonlinear fields and  $\omega$  was equal to 2, as used by Yee, for the linearly degenerate fields and zero for the nonlinear ones. (23:28)

Lastly the grid file is defined. Again, the same grid was used for all cases in this study.

As a final note, if the original version of ATEC is to be run at high temperatures, using a temperature corrected value of  $\gamma_a$  rather than the ideal gas value of 1.4,  $\gamma_a$  should be added as an input rather than 'hard wired' into the code. This would save having to edit and recompile for different temperatures.

The following are sample CASIN files for the two versions

Sample CASIN for ANTEC

320.24e4 2798.41 (PtINF, TtINF)  
49.2 (BETA2)  
58.96e4 (P3)  
2 10003  
0.95 (CFL, LOCAL)  
2 (METHOD: 1=Roe, 2=ULT1C)  
177 20 0 (IMAX, JMAX, IDIS)  
79 99 40 138 (IPER1, IPER2, ITE1, ITE2)  
0.0 0.0 0.0 0.0 0.0 (EPSILON 1, 2, 3, 4 and 5)  
2.0 2.0 2.0 0.0 0.0 (OMEGA 1, 2, 3, 4 and 5)  
blntgrd (GRID FILE)

Sample CASIN for the original ATEC

311.30e4 2714.37 (PtINF, TtINF)  
49.2 (BETA2)  
58.965e4 (P3)  
2 7001  
0.95 (CFL, LOCAL)  
2 (METHOD: 1=Roe, 2=ULT1C)  
177 20 0 (IMAX, JMAX, IDIS)  
79 99 40 138 (IPER1, IPER2, ITE1, ITE2)  
0.0 0.0 0.0 0.0 (EPSILON 1, 2, 3 and 4)  
0.0 2.0 0.0 2.0 (OMEGA 1, 2, 3 and 4)  
blntgrd (GRID FILE)

## Bibliography

1. Anderson, D. A., Tannehill, J. C., and Pletcher, R. H. Computational Fluid Mechanics and Heat Transfer, New York: Hemisphere Publishing Corporation, 1984.
2. Anderson, John D. Jr. Hypersonic and High Temperature Gas Dynamics, New York: McGraw-Hill Book Company, 1989.
3. Blackman, V. "Vibrational Relaxation in Oxygen and Nitrogen," Journal of Fluid Mechanics, 1: 61-85 (May 1956).
4. Beran, P. S. Class handouts distributed in AE 752, Computational Fluid Mechanics. School of Engineering, Air Force Institute of Technology (AU), Wright-Patterson AFB OH, Spring Quarter 1991.
5. Beran, P. S., Professor. Personal interviews. Air Force Institute of Technology (AU), Wright-Patterson AFB OH, February through November 1991.
6. Boletis, E. and Sieverding, C. H. "Experimental Study of Three-Dimensional Flow Field in a Turbine Stator Preceded by a Full Stage," Journal of Turbomachinery, 113: 1-9, (January 1991).
7. Driver, M. and Beran, P. "Analysis of Transonic Turbine Rotor Cascade Flows Using a Finite-Volume Total Variation Diminishing (TVD) Scheme," AIAA Paper No. 90-2127, July 1990.
8. Driver, Capt M., Phd Candidate. Personal interviews. Air Force Institute of Technology (AU), Wright-Patterson AFB OH, February through November 1991.
9. Dunn, M. G. "Phase and Time-Resolved Measurements of Unsteady Heat Transfer and Pressure in a Full-Stage Rotating Turbine," Journal of Turbomachinery, 112: 531-538, July 1990.
10. Emanuel, G. Gasdynamics: Theory and Applications, New York: American Institute of Aeronautics and Astronautics, 1986.
11. Gaydon, A. G. and Hurle, I. R. The Shock Tube in High-Temperature Chemical Physics. New York: Reinhold Publishing Corporation, 1963.
12. Harten, A. "Resolution Schemes for Hyperbolic Conservation Laws," Journal of Computational Physics, 49: 357-393 (1983).
13. Hertzberg, A. "The Application of the Shock Tube to the Study of the Problems of Hypersonic Flight," Jet Propulsion: Journal of the American Rocket Society, 26 No. 7: 549-554, July 1956.
14. Lambert, J. D. Vibrational and Rotational Relaxation in Gases, Oxford: Clarendon Press, 1977.
15. Liu, Y. and Vinokur, M. "Nonequilibrium Flow Computations I. An Analysis of Numerical Formulations of Conservation Laws," NASA Contractor Report 177489, Contract NAS2-11555, June 1988.

16. Moran, Capt K. J. "A Comparison of Molecular Vibration Modeling for Thermal Nonequilibrium Airflow." MS thesis, AFIT/GAE/ENY/90D-17. School of Engineering, Air Force Institute of Technology (AU), Wright-Patterson AFB OH, December 1990.
17. Moran, Capt K. J. "TVD Schemes for Thermal and Chemical Nonequilibrium Flows," Report for AE 899. School of Engineering, Air Force Institute of Technology (AU), Wright-Patterson AFB OH, Spring 1991.
18. Park, C. Nonequilibrium Hypersonic Aerothermodynamics. New York: John Wiley & Sons, 1990.
19. Park, C. and Yoon, S. "A Fully-Coupled Implicit Method for Thermo-Chemical Nonequilibrium Air at Sub-Orbital Flight Speeds," AIAA Paper No. 89-1974, June 1989.
20. Pratt & Whitney Aircraft Group Aeronautical Vest-Pocket Handbook. December 1977.
21. Stabe, R. G. and Whitney, W. J. "Performance of a High-Work Low Aspect Ratio Turbine Test with Realistic Inlet Radial Temperature Profile," AIAA Paper No. 84-1161, June 1984.
22. Vincenti, W. G. and Kruger, C. H., Jr. Introduction to Physical Gas Dynamics. Malabar, Florida: Robert E. Krieger Publishing Company, 1986.
23. Warming, R. F. and Beam, R. M. "On the Construction and Application of Implicit Factored Schemes for Conservation Laws," SIAM-AMS Proceedings, II: 85-129, 1978
24. Wright, J. K. Shock Tubes. New York: John Wiley & Sons Inc, 1961.
25. Yee, H. C. "A Class of High-Resolution Explicit and Implicit Shock-Capturing Methods," NASA TM-101088, February 1989.
26. Zucrow, M. J. and Hoffman, J. D. Gas Dynamics; Volume I, New York: John Wiley & Sons, 1976.

December 1991

Master's Thesis

THERMAL NONEQUILIBRIUM EFFECTS ON  
TURBINE CASCADE AERODYNAMICS

Jill L. R. Shaw, Captain, USAF

Air Force Institute of Technology, WPAFB OH 45433-6583

AFIT/GAE/ENY/91D-25

Mr Robert Gray  
WL/POTC  
Wright-Patterson AFB OH 45433-6563

Approved for public release; distribution unlimited

The AFIT Total Variation Diminishing Euler Code (ATEC) was modified to include a thermal nonequilibrium model to investigate high-temperature effects associated with vibrational relaxation in a transonic turbine cascade. Incorporation of this model into ATEC and creating ANTEC (AFIT Nonequilibrium TVD Euler Code) was accomplished in three phases. Steady-state solutions obtained with ANTEC were compared with those obtained with ATEC for various inlet and exit conditions. The CFL criterion was held constant in ATEC; however, it required variation for ANTEC. Blade temperature profiles, temperature difference contours in the vicinity of the trailing edge and the value of  $\gamma$  along the blade were analyzed. Even when corrected for high temperatures, the assumptions of a calorically perfect gas and thus a constant value of  $\gamma$  are inaccurate due to the temperature dependent nature of  $c_p$  and  $c_v$ . Maximum temperature differences of -741K and 539K were found near the trailing edge for the highest temperature case, with differences being most noticeable through the expansion at the trailing edge on the pressure surface and across the shocks from both surfaces. The vibrational relaxation model showed limitations at low temperatures.

Compressible Flow, Computational Fluid Dynamics, Transonic Flow,  
Turbine Cascade, Nonequilibrium Flow, Vibrational Relaxation

70

Unclassified

Unclassified

Unclassified

UL

## GENERAL INSTRUCTIONS FOR COMPLETING SF 298

The Report Documentation Page (RDP) is used in announcing and cataloging reports. It is important that this information be consistent with the rest of the report, particularly the cover and title page. Instructions for filling in each block of the form follow. It is important to **stay within the lines to meet optical scanning requirements.**

### **Block 1. Agency Use Only (Leave Blank)**

**Block 2. Report Date.** Full publication date including day, month, and year, if available (e.g. 1 Jan 88). Must cite at least the year.

**Block 3. Type of Report and Dates Covered.** State whether report is interim, final, etc. If applicable, enter inclusive report dates (e.g. 10 Jun 87 - 30 Jun 88).

**Block 4. Title and Subtitle.** A title is taken from the part of the report that provides the most meaningful and complete information. When a report is prepared in more than one volume, repeat the primary title, add volume number, and include subtitle for the specific volume. On classified documents enter the title classification in parentheses.

**Block 5. Funding Numbers.** To include contract and grant numbers; may include program element number(s), project number(s), task number(s), and work unit number(s). Use the following labels:

<b>C</b> - Contract	<b>PR</b> - Project
<b>G</b> - Grant	<b>TA</b> - Task
<b>PE</b> - Program Element	<b>WU</b> - Work Unit Accession No.

**Block 6. Author(s).** Name(s) of person(s) responsible for writing the report, performing the research, or credited with the content of the report. If editor or compiler, this should follow the name(s).

**Block 7. Performing Organization Name(s) and Address(es).** Self-explanatory.

**Block 8. Performing Organization Report Number.** Enter the unique alphanumeric report number(s) assigned by the organization performing the report.

**Block 9. Sponsoring/Monitoring Agency Names(s) and Address(es).** Self-explanatory.

**Block 10. Sponsoring/Monitoring Agency Report Number.** (If known)

**Block 11. Supplementary Notes.** Enter information not included elsewhere such as: Prepared in cooperation with...; Trans. of ..., To be published in .... When a report is revised, include a statement whether the new report supersedes or supplements the older report.

### **Block 12a. Distribution/Availability Statement.**

Denote public availability or limitation. Cite any availability to the public. Enter additional limitations or special markings in all capitals (e.g. NOFORN, REL, ITAR)

**DOD** - See DoDD 5230.24, "Distribution Statements on Technical Documents."

**DOE** - See authorities

**NASA** - See Handbook NHB 2200.2.

**NTIS** - Leave blank.

### **Block 12b. Distribution Code.**

**DOD** - DOD - Leave blank

**DOE** - DOE - Enter DOE distribution categories from the Standard Distribution for Unclassified Scientific and Technical Reports

**NASA** - NASA - Leave blank

**NTIS** - NTIS - Leave blank.

**Block 13. Abstract.** Include a brief (Maximum 200 words) factual summary of the most significant information contained in the report.

**Block 14. Subject Terms.** Keywords or phrases identifying major subjects in the report.

**Block 15. Number of Pages.** Enter the total number of pages.

**Block 16. Price Code.** Enter appropriate price code (NTIS only).

### **Blocks 17. - 19. Security Classifications.**

Self-explanatory. Enter U.S. Security Classification in accordance with U.S. Security Regulations (i.e., UNCLASSIFIED). If form contains classified information, stamp classification on the top and bottom of the page.

**Block 20. Limitation of Abstract.** This block must be completed to assign a limitation to the abstract. Enter either UL (unlimited) or SAR (same as report). An entry in this block is necessary if the abstract is to be limited. If blank, the abstract is assumed to be unlimited.